A&A 555, A95 (2013)
DOI: 10.1051/0004-6361/201321203


Astronomy & Astrophysics

# GRO J1008−57: an (almost) predictable transient X-ray binary⋆

M. Kühnel[1], S. Müller[1], I. Kreykenbohm[1], F. Fürst[2], K. Pottschmidt[3,4], R. E. Rothschild[5], I. Caballero[6], V. Grinberg[1], G. Schönherr[7], C. Shrader[4,8], D. Klochkov[9], R. Staubert[9], C. Ferrigno[10], J.-M. Torrejón[11], S. Martínez-Núñez[11], and J. Wilms[1]

[1] Dr. Karl Remeis-Observatory & ECAP, Universität Erlangen-Nürnberg, Sternwartstr. 7, 96049 Bamberg, Germany
e-mail: matthias.kuehnel@sternwarte.uni-erlangen.de
[2] Space Radiation Lab, California Institute of Technology, MC 290-17 Cahill, 1200 E. California Blvd., Pasadena, CA 91125, USA
[3] CRESST, Center for Space Science and Technology, UMBC, Baltimore, MD 21250, USA
[4] NASA Goddard Space Flight Center, Greenbelt, MD 20771, USA
[5] Center for Astronomy and Space Sciences, University of California, San Diego, La Jolla, CA 92093, USA
[6] CEA Saclay, DSM/IRFU/SAp – UMR AIM (7158) CNRS/CEA/Université Paris 7, Diderot, 91191 Gif sur Yvette, France
[7] Leibniz-Institut für Astrophysik Potsdam, An der Sternwarte 16, 14482 Potsdam, Germany
[8] Universities Space Research Association, Columbia, MD 21044, USA
[9] Institut für Astronomie und Astrophysik, Universität Tübingen, Sand 1, 72076 Tübingen, Germany
[10] ISDC Data Center for Astrophysics, Chemin d'Écogia 16, 1290 Versoix, Switzerland
[11] Instituto de Física Aplicada a las Ciencias y las Tecnologías, Universidad de Alicante, 03080 Alicante, Spain

Received 31 January 2013 / Accepted 9 May 2013

**ABSTRACT**

A study of archival RXTE, *Swift*, and *Suzaku* pointed observations of the transient high-mass X-ray binary GRO J1008−57 is presented. A new orbital ephemeris based on pulse arrival-timing shows the times of maximum luminosities during outbursts of GRO J1008−57 to be close to periastron at orbital phase −0.03. This makes the source one of a few for which outburst dates can be predicted with very high precision. Spectra of the source in 2005, 2007, and 2011 can be well described by a simple power law with high-energy cutoff and an additional black body at lower energies. The photon index of the power law and the black-body flux only depend on the 15–50 keV source flux. No apparent hysteresis effects are seen. These correlations allow us to predict the evolution of the pulsar's X-ray spectral shape over all outbursts as a function of just one parameter, the source's flux. If modified by an additional soft component, this prediction even holds during GRO J1008−57's 2012 type II outburst.

**Key words.** X-rays: binaries – pulsars: individual: GRO J1008-57 – accretion, accretion disks – ephemerides

## 1. Introduction

GRO J1008−57 was discovered by CGRO during an X-ray outburst on 1993 July 14 (Wilson et al. 1994; Stollberg et al. 1993). It is a transient neutron star with a Be-star companion of type B0e (Coe et al. 1994) at a distance of 5.8 kpc (Riquelme et al. 2012). In these high-mass X-ray binaries (HMXBs) the compact object is on a wide eccentric orbit around its companion, which itself features a circumstellar disk due to its fast rotation. Periastron passages of the neutron star lead to accretion from the donor's decretion disk and regular X-ray outbursts. Based on RXTE-ASM measurements of the X-ray light curve, Levine & Corbet (2006, see also Levine et al. 2011) derived an orbital period of 248.9(5) d[1]. Since individual X-ray outbursts are relatively short, with durations of around 14 d, determining the parameters of the binary orbit is challenging. Coe et al. (2007) have derived an orbital solution (see Table 2) based on pulse-period folding of the 93.6 s X-ray period (Stollberg et al. 1993).

The hard X-ray spectrum of GRO J1008−57 was first studied by Grove et al. (1995) and Shrader et al. (1999). Above 20 keV the spectrum can be well described by an exponentially cutoff power law (Grove et al. 1995; Shrader et al. 1999; Coe et al. 2007). Below 20 keV, *Suzaku* observations show a complex spectrum with Fe line fluorescent emission and a power-law continuum (Naik et al. 2011).

A slight deviation from the continuum at 88 keV in CGRO-OSSE observations was interpreted by Shrader et al. (1999) as a possible cyclotron line feature, i.e., as a feature caused by inelastic scattering of photons off electrons quantized in the strong magnetic field at the neutron star's poles (Schönherr et al. 2007; Caballero & Wilms 2012; Pottschmidt et al. 2012, and references therein). Even if the 88 keV feature is the second harmonic cyclotron line, as argued by Shrader et al. (1999), GRO J1008−57 would be one of the most strongly magnetized neutron stars in an accreting system to date.

In this paper we present an analysis of archival observations of GRO J1008−57 with RXTE, *Suzaku*, and *Swift*. Section 2 presents the data analysis strategy. In Sect. 3 an updated orbital solution based on data from outbursts in 2005 and 2007 is presented. The X-ray spectrum of GRO J1008−57 is discussed in

⋆ Table 1 is available in electronic form at http://www.aanda.org
[1] The error bars are given in units of the last digit shown.

Sect. 4 and the spectroscopic results are applied and compared in Sect. 5. The paper closes with a summary and conclusions in Sect. 7.

## 2. Observations and data reduction

Data from five outbursts of GRO J1008−57 were analyzed. The earliest outburst studied here occurred in 2005 February and was well covered by pointed RXTE observations (Fig. 1). In 2007 December, GRO J1008−57 underwent its strongest outburst during the lifetime of the RXTE-All Sky Monitor. The 2–10 keV peak flux was 84(5) mCrab (Fig. 1). Except for the rise, the whole outburst was observed regularly by RXTE. *Swift* recorded the source around maximum intensity and *Suzaku* during its decay. During 2011 April we triggered RXTE observations to cover the start of the third outburst analyzed here. Later outbursts in 2011 December and 2012 were covered by a few *Swift* observations each. In addition, to measure the diffuse emission from the region, we used data from an RXTE observation campaign in 1996/1997 that were collected while the source was off. Table 1 lists a log of the observations.

The binary orbital phases of the 2005, 2007, and 2011 April observations are shown in Fig. 2. Outbursts occurred around the periastron of the orbit, where mass accretion from the circumstellar disk is possible.

In the following the instruments used in the analysis of these outbursts are described. All spectral and timing modeling was performed with the Interactive Spectral Interpretation System (ISIS, Houck & Denicola 2000, version 1.6.2–7). Unless otherwise stated, all error bars are given at the 90% level for each parameter of interest.

### 2.1. RXTE

The Proportional Counter Array (PCA, Jahoda et al. 2006) was one of two pointed instruments onboard the *Rossi* X-ray Timing Explorer (RXTE) and was sensitive for X-rays between 2 and 90 keV. The PCA consisted of five Proportional Counter Units (PCUs), collimated to a field of view of ∼1°. Unless stated otherwise, only data from PCU2 were used, which was the best-calibrated PCU (Jahoda et al. 2006). Since the source can be weak away from the outburst peak, only data from the top layer of PCU2 were used. Data were reduced using HEASOFT 6.11 and using standard data reduction pipelines (Wilms et al. 2006). Light curves for the timing analysis were extracted using barycentered GoodXenon data with 1 s time resolution. For spectral analysis, 4.5 keV–50 keV PCA data were used to avoid calibration problems around the Xenon L-edge. Data from 10–20 keV, 20–30 keV, 30–40 keV, and >40 keV were rebinned by a factor of 2, 4, 6, and 8, respectively. In addition, systematic uncertainties of 0.5% were added to the spectra (Jahoda et al. 2006). To compensate for the few percent uncertainty of the PCA background model, the background was scaled with a multiplicative factor.

Hard X-ray RXTE data were obtained using the High Energy X-ray Timing Experiment (HEXTE, Rothschild et al. 1998). HEXTE consisted of two clusters A and B of four NaI/CsI scintillation detectors, alternating between the source and background positions ("rocking"). In 2006 October, the rocking of cluster A was turned off and the detector was fixed in on-source position due to an anomaly in the rocking mechanism. Because no reliable background estimates are available, cluster A was not used for spectral analysis of the post 2006 data. The rocking of cluster B was switched off in 2010 April, therefore no

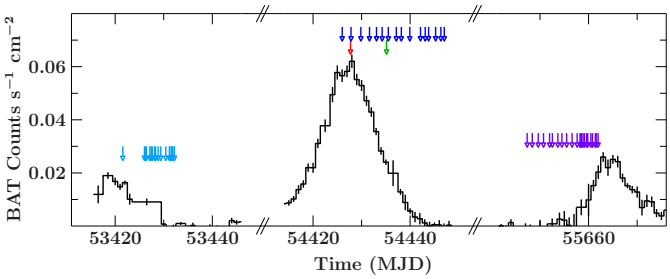


**Fig. 1.** *Swift*-BAT light curve around the outbursts in 2005, 2007, and 2011 April. The vertical arrows at the top mark the start times of individual observations of RXTE (light, dark blue, and purple), *Swift* (red), and *Suzaku* (green).

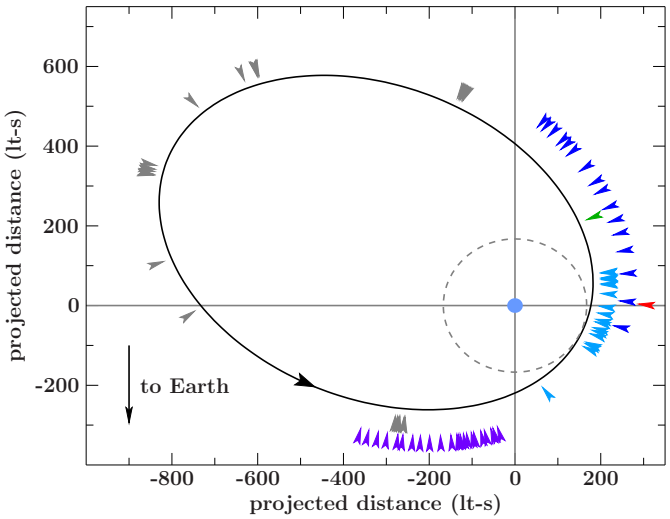


**Fig. 2.** Projected orbital plane of the binary. The reference frame is centered on the optical companion, whose size is set to 7 $R_\odot$ (Coe et al. 2007). The dashed circle sketches a circumstellar disk of 72 $R_\odot$ as proposed by Coe et al. (2007). Orbital phases of the observations from 2005, 2007, and 2011 April are marked by arrows. The colors are the same as in Fig. 1. Gray arrows represent RXTE observations obtained in quiescence (Obsids 20132-* and 20123-*). Orbital phases are calculated using the ephemeris given in Table 2.

HEXTE data were used for analysis during the 2011 April outburst. 20–100 keV HEXTE data were used for spectral analysis and rebinned by a factor of 2, 3, 4, and 10 in the energy intervals 20–30 keV, 30–45 keV, 45–60 keV, and >60 keV, respectively.

The analysis of the GRO J1008−57 data is complicated because of the low Galactic latitude of the source ($b = -1.^\circ827$). At such low latitudes, the cumulative effect of the Galactic ridge emission in the ∼1° radius field of view of the PCA is strong enough to lead to visible features in the X-ray spectrum. When comparing simultaneous PCA measurements with those from imaging instruments, these features mainly show up as excess emission in the Fe K$\alpha$ band around 6.4 keV and a slight difference in the continuum shape (e.g., Müller et al. 2012). The Galactic ridge emission is believed to originate from many unresolved X-ray binaries in the field of view (Revnivtsev et al. 2009) and can be empirically modeled by the sum of a bremsstrahlung continuum and iron emission lines from neutral, helium-like, and hydrogenic iron (Ebisawa et al. 2007; Yamauchi et al. 2009). Owing to the energy resolution of the PCA, the three lines merge into a blended emission line.

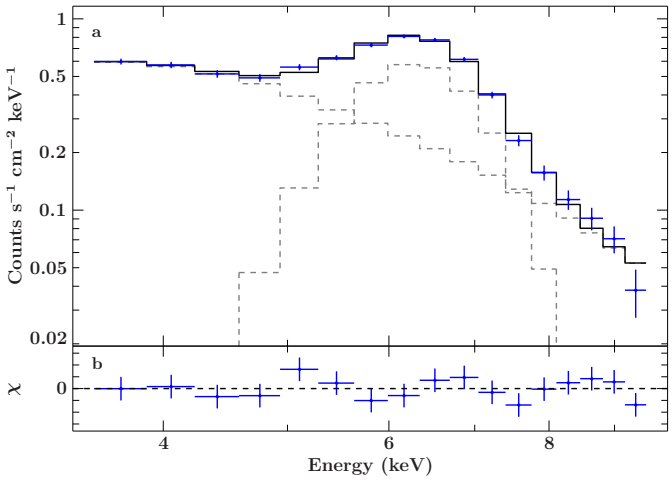


**Fig. 3.** Galactic ridge emission in the region around GRO J1008−57 as measured by RXTE-PCA during a quiescent state of the source. **a)** The spectrum shows clear fluorescence emission of iron, which can be modeled by a broad Gaussian centered at 6.4 keV, and a bremsstrahlung component. **b)** Model residuals.

The Galactic ridge emission shows a strong spatial variability. Fortunately, GRO J1008−57 was observed by RXTE in 1996 and 1997 during a quiescent state (proposal IDs 20132 and 20123). The PCA light curves from these observations do not show any evidence for pulsed emission between 91 and 96 s. Figure 3 shows the 181 ks spectrum accumulated from these observations. In the spectral analysis, this component was modeled as the sum of a bremsstrahlung continuum and three Fe K lines and is only present in the PCA data (the ridge emission is too soft to influence HEXTE).

### 2.2. Swift

To analyze the *Swift* observations, data from its X-ray Telescope (XRT) were used (Gehrels et al. 2004). The 1.5–9 keV spectra were extracted in the windowed-timing mode, a fast CCD readout mode that prevents pile-up for sources up to 600 mCrab. Only the observations after the 2011 December outburst and obs. 00031030013 before the giant outburst of 2012 October/November were extracted in the photon-counting mode. Source spectra were obtained from a 1′ radius circle centered on the source, or an annular circular region if pile-up was present. Background spectra were accumulated from two circular regions off the source position with radii up to ∼1.′5. Unless stated otherwise, spectral channels were added until a minimum signal-to-noise ratio of 20 was achieved. The light curve was extracted with 1 s time resolution.

### 2.3. Suzaku

Similar to *Swift*-XRT, the X-ray Imaging Spectrometer (XIS) mounted on the *Suzaku* satellite uses Wolter telescopes to focus the incident X-rays (Koyama et al. 2007). After correcting the spacecraft attitude (Nowak et al. 2011), we accumulated normal-clock mode 1–9 keV data in 1/4 window from front-illuminated CCDs XIS0 and XIS3 and from the back-illuminated XIS1 were accumulated from annular circular extraction regions with 1.′5 radius. CCD areas with more than 4% pile-up (Nowak et al. 2011) were excluded. Depending on source brightness, the circular exclusion region had a radius of typically 0.′5. The energy ranges 1.72 keV–1.88 keV and 2.19 keV–2.37 keV were ignored because of calibration problems around the Si- and Au-edges (Nowak et al. 2011). For the back illuminated XIS1, the energy range in between the edges (1.88 keV–2.19 keV) was ignored as well because of significant discrepancies to the front-illuminated XIS0 and XIS3. The spectral channels of XIS were added such that a combined signal-to-noise ratio of 40 was achieved. For timing analysis, XIS3-light curves with 2 s resolution were used.

*Suzaku*'s collimated hard X-ray detector (HXD; Takahashi et al. 2007) can be used to detect photons from 10 keV up to 600 keV. It consists of two layers of silicon PIN diodes for energies below 50 keV above phoswich counters sensitive >57 keV (GSO). Spectra from the energy ranges of 12–50 keV (PIN) and 57–100 keV (GSO) were used. The PIN energy channels were binned to achieve a signal-to-noise ratio of 20. For the GSO spectrum, a binning factor of 2 was applied to channels between 60 keV and 80 keV and of 4 for higher energies.

Note that the pile-up in the 2007 XIS data described above was not taken into account in the previous analysis of these data by Naik et al. (2011). If one does not excise the high count region of the core of the point spread function, photons that arrive in the same or adjacent pixels are misinterpreted by the detection chain as one photon of higher energy. If the joint XIS/HXD spectra are then modeled, this spectral distortion results in the apparent appearance of soft spectral components claimed by Naik et al. (2011). These components are therefore not present in the real source spectrum.

## 3. Orbit of GRO J1008−57

### 3.1. Orbit determination using pulse-arrival time measurements

Between the 2007 outburst and the reported periastron passage of the original orbit determination by Coe et al. (2007) using CGRO-BATSE, GRO J1008−57 orbited its companion 21 times. The accumulated uncertainty of the ephemeris reported in Coe et al. (2007) during this time is about 8.5 d (0.03 $P$), or almost as long as a typical outburst of the source. Not correcting for this uncertainty in the analysis of the pulsar's spin could introduce false spin-up/spin-down phases.

To derive the orbit of GRO J1008−57 we used the pulse arrival-timing method (see also Deeter et al. 1981; Boynton et al. 1986, and references therein). Assuming a neutron star with a slowly varying pulse period, the arrival time $t(n)$ of the $n$th pulse is given using a Taylor expansion of the pulse ephemeris up to the third order,

$$t(n) = t_0 + P_0 n + \frac{1}{2!} P_0 \dot{P} n^2 + \frac{1}{3!}\left(P_0^2 \ddot{P} + P_0 \dot{P}^2\right) n^3 + \frac{a_x \sin i}{c} F(e, \omega, \tau, \theta), \quad (1)$$

where $P_0$ is the pulse period in the rest frame of the neutron star at the reference time $t_0$, $a_x \sin i$ is the projected semi-major axis of the neutron star's orbit, and $\dot{P}$ and $\ddot{P}$ are the changes in the spin period. The function $F$ describes the time delay due to an orbit of eccentricity $e$, longitude of periastron $\omega$, time of periastron passage $\tau$, and mean anomaly $\theta$. The latter is connected to the orbital period $P_{\rm orb}$ via $\theta = 2\pi(t - \tau)/P_{\rm orb}$ (see also Kelley et al. 1980; Nagase 1989). Note that for reasons of computational speed and numerical accuracy, $t(n)$ should be evaluated using a Horner (1819) scheme.

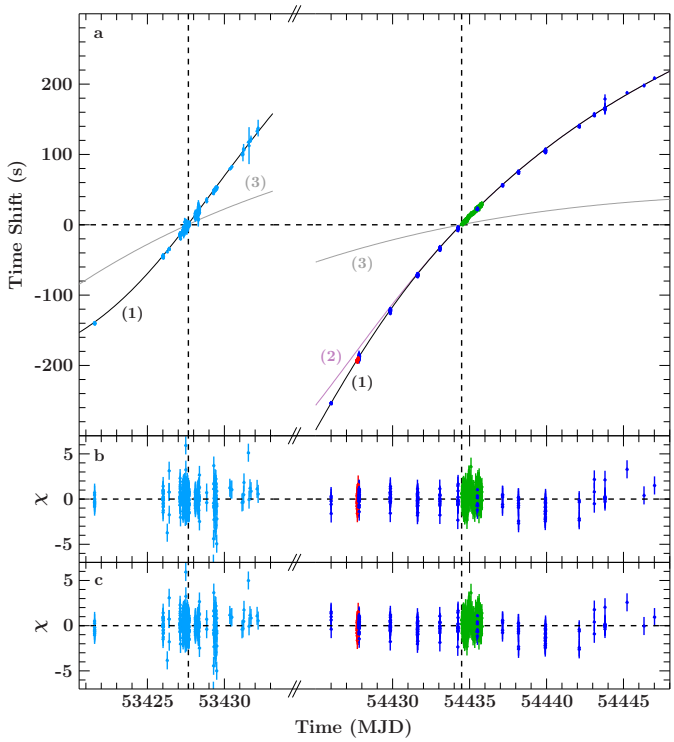


**Fig. 4.** **a)** Time shifts relative to a constant pulse period for the 2005 and 2007 outbursts from RXTE- (light blue: 2005, dark blue: 2007), *Swift*- (red) and *Suzaku*-data (green). The arbitrary reference time for the pulse ephemeris is indicated by the vertical dashed lines. The gray curve (3) shows the effect of the orbital correction using the orbit of Coe et al. (2007) on the arrival times. The best-fit pulse ephemeris based on the revised orbital parameters of Table 2 are shown in black with (1) and purple without a spin-up (2). **b)** Residuals of the model without taking the times of maximum source flux during outbursts into account. **c)** Residuals of the best-fit model (1).

To determine the pulse arrival times, a template pulse profile determined by folding part of an observation with a locally determined pulse period (Leahy et al. 1983) was correlated with the observed light curves. Note that an individual profile was created for each instrument used, so that changes in the profile shape caused by time evolution or by different energy ranges and responses of the detectors were taken into account.

After finding the arrival times, the difference between measured and predicted arrival time according to Eq. (1) was minimized by varying the orbital parameters as well as $P_0$, $\dot{P}$, and $\ddot{P}$ using a standard $\chi^2$ minimization algorithm. Since the template pulse profile depends on the orbit correction and pulse ephemeris, i.e., on the fit parameters, the whole process was iterated until convergence was reached.

### 3.2. Orbit of GRO J1008−57

To determine the orbit of GRO J1008−57 all data available from the 2005 and 2007 outbursts were used. Template pulse profiles have 32 phase bins. During the 2005 outburst a period of $P_{\rm obs}$ = 93.698(7) s was found, while for the 2007 one the period is $P_{\rm obs}$ = 93.7369(12) s. The reference time needed to determine the time shifts was set to the first time bin of the *Suzaku*-light curve (MJD 54 434.4819) for data taken in 2007, and to the first time bin of RXTE-observation 90089-03-02-00 (MJD 53 427.6609) for the 2005 outburst. See Fig. 5 for example pulse profiles.

**Table 2.** Pulse periods and orbital parameters as determined by Coe et al. (2007) and in this paper.

| | |
|---|---|
| Coe et al. (2007) | |
| Eccentricity | $e = 0.68(2)$ |
| Projected semi-major axis | $a \sin i = 530(60)$ lt-s |
| Longitude of periastron | $\omega = -26(8)^\circ$ |
| Orbital period | $P_{\rm orb} = 247.8(4)$ d |
| Time of periastron passage | $\tau$ = MJD 49 189.8(5) |
| This paper | |
| Orbital period | $P_{\rm orb} = 249.48^{+0.04}_{-0.04}$ d |
| Time of periastron passage | $\tau$ = MJD $54\,424.71^{+0.20}_{-0.16}$ |
| Spin period during 2005 | $P_{2005} = 93.67928^{+0.00010}_{-0.00009}$ s |
| Spin period during 2007 | $P_{2007} = 93.71336^{+0.00017}_{-0.00022}$ s |
| Spin-up before MJD 54 434.4819 | $\dot{P}_{2007} = -0.61^{+0.24}_{-0.22} \times 10^{-9}$ s s$^{-1}$ |
| | $\ddot{P}_{2007} = 3.38^{+0.07}_{-0.16} \times 10^{-14}$ s s$^{-2}$ |

**Notes.** The parameters $e$, $a \sin i$, and $\omega$ remain unchanged in the analysis presented here. Uncertainties of the new values are at the 90% confidence level ($\chi^2_{\rm red}$ = 1.04 for 1024 d.o.f.).

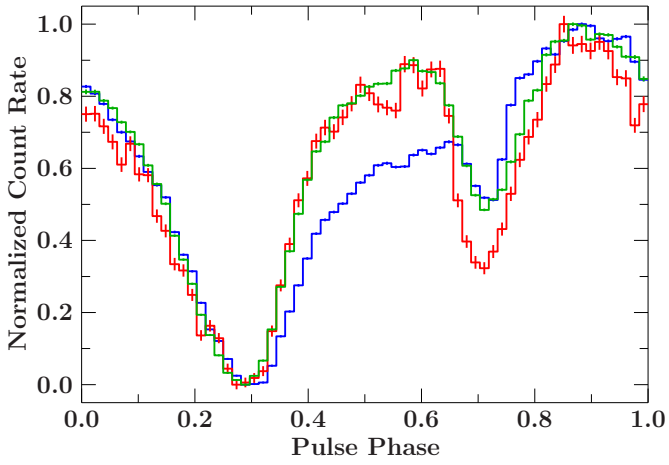


**Fig. 5.** RXTE-PCA (blue), *Swift*-XRT (red), and *Suzaku*-XIS3 pulse profiles (green). The profiles are folded on the first time bin of the extracted XIS3 light curve (MJD 54 434.4819). Owing to a comparable sensitive energy range the profiles as detected by *Swift*-XRT (0.2–10 keV) and *Suzaku*-XIS3 (0.2–12 keV) are similar in shape, while the secondary peak is much more prominent at higher energies as seen in RXTE-PCA (2–60 keV). To show the good agreement between the *Swift* and *Suzaku* data, profiles are shown with 64 bins instead of the 32 bins used for the arrival time analysis.

Figure 4 shows the difference between the measured pulse arrival times and a pulse ephemeris, which assumes constant pulse periods with values given above. Calculating the arrival time using the ephemeris of Coe et al. (2007, see Table 2) did not result in a good description of the data (Fig. 4, gray lines). In principle, the remaining difference could be explained by a very strong spin-up and spin-down. If the difference is explained in this way, the resulting orbital parameters are, however, inconsistent with the phasing of the outbursts seen with all sky monitors (see Sect. 3.3 below). The only orbital parameters that can result in the difference between the gray line in Fig. 4 and the data are the epoch of periastron passage, $\tau$, and the orbital period, $P_{\rm orb}$. A change in eccentricity, $e$, $\omega$, or $a \sin i$ shifts arrival times in a way that would move the lines in Fig. 4 up and down or stretch

the whole figure. Neither change results in a good description of the data. Holding all parameters except $P_0$, $\tau$, and $P_{\rm orb}$ fixed, and performing a $\chi^2$ minimization then results in a good description of all arrival times (Fig. 4, black and purple curves).

Close inspection of the best fit revealed a deviation between the best fit and the data from the early measurements during the 2007 outburst, however, which were taken during the maximum of the outburst. This discrepancy at high luminosities during the 2007 outburst can be explained by assuming that during this phase the pulsar underwent a spin-up, i.e., $\dot{P} \neq 0\,\mathrm{s\,s^{-1}}$ and $\ddot{P} \neq 0\,\mathrm{s\,s^{-2}}$, between MJD 54 426 and MJD 54 434. This approach is not unreasonable since high-luminosity phases are coincident with a high angular momentum transfer onto the neutron star, which has been detected in other transient X-ray binaries as well, e.g., A0535+26 (Camero-Arranz et al. 2012).

Using the resulting orbital parameters, a first inspection of the orbital phases where the outbursts of GRO J1008−57 are detected in RXTE-ASM and *Swift*-BAT showed that the times of maximum source flux are consistent with a single orbital phase (see Sect. 3.3). To enhance the orbital parameter precision further, especially the orbital period, the times of maximum source flux were fitted simultaneously with the arrival times data. The residuals are very similar to those found previously (compare residual panels b and c of Fig. 4).

The best-fit parameters of the final orbital solution and pulse period ephemeris are presented in Table 2. Note that the simultaneous fit of the 2005 and 2007 arrival times data as well as the outburst times in ASM and BAT allow one to break the correlation between the orbital period and the time of periastron passage, which is generally found when studying pulse arrival-times from one outburst only.

### 3.3. ASM- and BAT-analysis

The orbital period of 249.48(4) d found by the combined pulse arrival-times and outburst times analysis in the previous section differs by more than $4\sigma$ from the value found by Coe et al. (2007, $P_{\rm orb} = 247.8(4)$ d) and by slightly more than $1\sigma$ from the orbital period found by Levine & Corbet (2006, $P_{\rm orb} = 248.9(5)$ d) from the RXTE-ASM light curves. Since outbursts occur during each periastron passage, $P_{\rm orb}$ can also be determined by measuring the time of peak flux from the available RXTE-ASM and *Swift*-BAT data only as a consistency check. The average distance between outburst peaks is 249.7(4) d, which agrees with the results of the arrival time analysis of Sect. 3.2 and Levine & Corbet (2006).

After confirming the updated orbital period, it is possible to compare the time of maximum source flux with the periastron passages predicted by the revised orbital solution. With the exception of the bright 2007 outburst (see below), the results displayed in Fig. 6 show that outburst maxima are consistent with a mean orbital phase of $\phi_{\rm orb} = -0.0323(17)$ where the uncertainty includes the uncertainties of the orbital parameters. Thus, GRO J1008−57 reaches maximum luminosity during outburst very close to, but significantly before, periastron.

Following the improved orbital parameters and the detected phase shift between the peak flux and the periastron passage, the date of the highest flux of GRO J1008−57 during an outburst can be predicted:

$$T_{\rm max} = \mathrm{MJD\,54\,416.65} + n \times 249.48, \quad (2)$$

where $n$ is the number of orbits since the outburst in 2007. The uncertainty of $T_{\rm max}$ is about 3 d. It is mainly due to the scattering of the outburst times (Fig. 6). A successful prediction of the

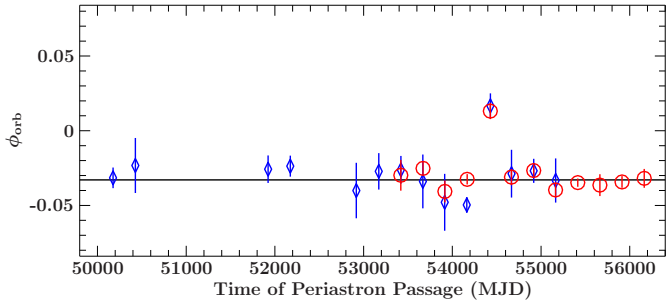


**Fig. 6.** Orbital phases of each detected outburst of GRO J1008−57 in ASM (blue) and BAT (red), determined from the orbital parameters found by the arrival time analysis (see text). The solid line shows the best-fit outburst phase of the ASM- and BAT-data. The outlier is the 2007 December outburst.

2011 April outburst resulted in the RXTE observations during the rise of this outburst, which are analyzed in this work.

The ASM analysis shows that the 2007 outburst of GRO J1008−57, the brightest outburst seen by RXTE-ASM, was delayed by ∼11 days compared with the standard ephemeris. The time of maximum luminosity from this outburst was therefore excluded from the analysis above. However, as the typical duration of one outburst of GRO J1008−57 is ∼14 days (0.056 $P_{\rm orb}$), even this outburst is clearly connected with a periastron passage of the neutron star.

## 4. Spectral modeling

### 4.1. Continuum of GRO J1008−57

The continuum emission of accreting neutron stars is produced in the accretion columns over the magnetic poles of the compact object (Becker & Wolff 2007, and references therein). Here, the kinetic energy of the infalling material is thermalized and a hot spot forms on the surface that is visible in the X-ray band as a black body. A fraction of that radiation is then Compton-upscattered in the accretion column above the hot spot, forming a hard power-law spectrum with an exponential cutoff at around 50–150 keV.

Although theoretical models now start to emerge that allow one to model the continuum emission directly (Becker & Wolff 2007; Ferrigno et al. 2009), these models are not yet self-consistent enough to describe the spectra of all accreting neutron stars. For this reason, empirical models are typically used (see Müller et al. 2013; and DeCesar et al. 2013 for recent summaries).

Owing to the mentioned exponential cutoff of the spectrum, data from instruments such as the CGRO-OSSE and -BATSE mainly show the exponential roll-over above 20 keV. As a result, the combined CGRO-OSSE and -BATSE spectrum (20–150 keV) during the discovery outburst of GRO J1008−57 in 1993 was initially described by a bremsstrahlung continuum (Shrader et al. 1999). As discussed by Shrader et al. (1999) for the joint 1993 CGRO/*ASCA*-GIS (0.7–10 keV) spectrum and also by Coe et al. (2007) for *INTEGRAL* data from the 2004 June outburst, the soft X-ray spectrum cannot be described by a bremsstrahlung continuum. Instead, a power-law spectrum with an exponential cutoff of the form

$$\mathtt{CUTOFFPL}(E) \propto E^{-\Gamma} \mathrm{e}^{-E/E_{\rm fold}} \quad (3)$$

was found to be a good description of the spectrum. Here $\Gamma$ is the photon index and $E_{\rm fold}$ the folding energy.

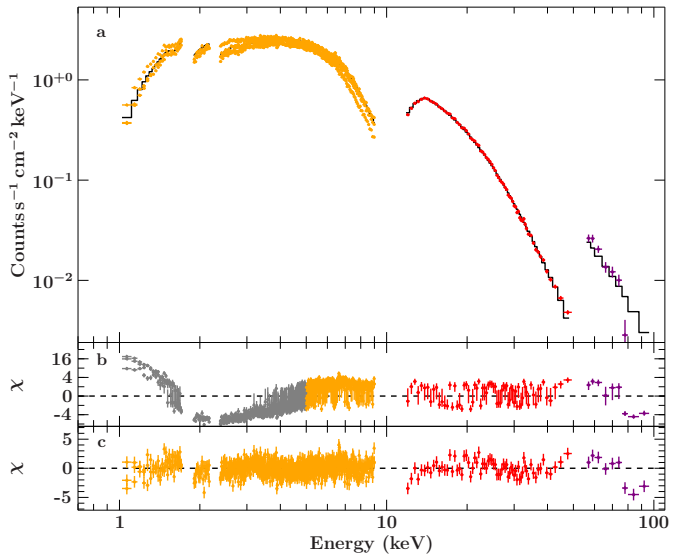


**Fig. 7. a)** 2007 *Suzaku*-spectrum of GRO J1008−57 (XISs: orange, PIN: red, GSO: purple). Spectral channels are rebinned for display purposes. **b)** A pure CUTOFFPL-model fitted to data above 5 keV, to compare with *INTEGRAL*-data (Coe et al. 2007), results in a poor description below that energy (gray residuals). **c)** Adding a black body and a narrow iron line, and taking absorption in the interstellar medium into account, improves the fit to $\chi^2_{\rm red} \sim 1.12$ (1845 d.o.f.).

Applying this model to the 2007 *Suzaku* data gives a good description of the spectrum above ∼5 keV (Fig. 7a). At softer energies deviations are present. Note that these differences are not the same as those caused by pile-up discussed in Sect. 2.3. The broad band deviations are well described by a black-body spectrum modified by interstellar absorption. A narrow iron K$\alpha$ fluorescence line at 6.4 keV is needed to achieve an acceptable fit with a reduced $\chi^2_{\rm red} = 1.14$ for 1896 degrees of freedom (d.o.f.; see Fig. 7). The iron K$\beta$ fluorescence line at 7.056 keV was included with an equivalent width fixed to 13% of the width of the K$\alpha$ line. This additional K$\beta$ line is included in all spectral fits in this paper. The $\chi^2$ can be further decreased to $\chi^2_{\rm red} = 1.11$ (1888 d.o.f.) by ignoring the GSO spectrum. The reason are residuals above 75 keV, which might be caused by the putative cyclotron line at 88 keV (Shrader et al. 1999). The signal quality does not allow one to constrain the cyclotron line parameters properly, however. See Sect. 4.3 for discussion of that feature. Adding the simultaneous RXTE spectrum (93032-03-03-01) to the *Suzaku* data and taking the Galactic ridge emission into account does not appreciably change the best-fit parameters. Table 3[2] lists the final best-fit parameters. Applying the same model to the quasi-simultaneous *Swift*-XRT, RXTE-PCA and RXTE-HEXTE data (RXTE obsid 93032-03-02-00) from the same 2007 outburst also gives a good description of the spectrum (see Fig. 8 and Table 3[2]).

In summary, the broad-band spectrum of GRO J1008−57 can be described by a model of the form

$$F_{\rm ph,model}(E) = \texttt{TBnew} \times (\texttt{CUTOFFPL} + \texttt{BBODY} + {\rm Fe}_{6.4\,\rm keV} + {\rm Fe}_{6.67\,\rm keV}) + [\rm GRE], \quad (4)$$

where $\rm Fe_{6.4\,keV}$ is a Gaussian emission line, BBODY describes a black body, and where the Galactic ridge emission is

$$\rm GRE = \texttt{TBnew} \times (\texttt{BREMSS} + Fe_{blend}), \quad (5)$$

[2] The parameters of the GRE are determined by a combined fit of all data from all outbursts and therefore listed in Table 4 (see Sect. 4.2).

**Table 3.** Best-fit continuum parameters of GRO J1008−57 determined from the simultaneous 2007 *Suzaku* and RXTE data ($\chi^2_{\rm red} = 1.15$, 1935 d.o.f.) and the quasi-simultaneous 2007 *Swift*-XRT and RXTE data ($\chi^2_{\rm red} = 1.15$, 160 d.o.f.).

| Component | | *Suzaku* RXTE | *Swift* RXTE | Unit |
|---|---|---|---|---|
| TBnew | $N_{\rm H}$ | $1.523^{+0.029}_{-0.029}$ | $1.56^{+0.17}_{-0.17}$ | $10^{22}$ cm$^{-2}$ |
| CUTOFFPL[a] | $\Gamma$ | $0.522^{+0.024}_{-0.024}$ | $0.57^{+0.07}_{-0.07}$ | |
| | $E_{\rm fold}$ | $15.6^{+0.5}_{-0.4}$ | $16.1^{+0.8}_{-0.8}$ | keV |
| | $F_{\rm PL}$ | $1.982^{+0.029}_{-0.029}$ | $3.97^{+0.08}_{-0.08}$ | $10^{-9}$ erg s$^{-1}$ cm$^{-2}$ |
| BBODY[a] | $kT$ | $1.854^{+0.025}_{-0.025}$ | $1.86^{+0.06}_{-0.05}$ | keV |
| | $F_{\rm BB}$ | $0.501^{+0.016}_{-0.016}$ | $0.77^{+0.08}_{-0.08}$ | $10^{-9}$ erg s$^{-1}$ cm$^{-2}$ |
| Iron line | $E$ | 6.4 (fix) | | keV |
| | $\sigma$ | $10^{-6}$ (fix) | | keV |
| | $W$ | $23.5^{+2.5}_{-2.5}$ | $41^{+10}_{-10}$ | eV |
| Constants[b] | $c_{\rm HEXTE}$ | $0.84^{+0.04}_{-0.04}$ | $0.853^{+0.019}_{-0.019}$ | |
| | $c_{\rm XRT}$ | – | $0.809^{+0.010}_{-0.010}$ | |
| | $c_{\rm XIS0}$ | $0.804^{+0.007}_{-0.006}$ | – | |
| | $c_{\rm XIS1}$ | $0.845^{+0.007}_{-0.007}$ | – | |
| | $c_{\rm XIS3}$ | $0.801^{+0.006}_{-0.006}$ | – | |
| | $c_{\rm PIN}$ | $0.929^{+0.012}_{-0.010}$ | – | |
| | $c_{\rm GSO}$ | $1.15^{+0.10}_{-0.10}$ | – | |
| | $b_{\rm PCA}$ | $0.93^{+0.05}_{-0.05}$ | $0.96^{+0.04}_{-0.04}$ | |

**Notes.** The fit takes Galactic ridge emission applied to RXTE-PCA into account. The given uncertainties are at the 90%-confidence limit. See Table 4 for the parameters of the Galactic ridge emission model. [(a)] $F_{\rm PL}$ and $F_{\rm BB}$ are unabsorbed fluxes, $F_{\rm PL}$ is the power-law flux in 15–50 keV, $F_{\rm BB}$ is the bolometric black-body flux. [(b)] Detector flux calibration constants, $c$, are given relative to the RXTE-PCA; the PCA background is multiplied by $b_{\rm PCA}$.

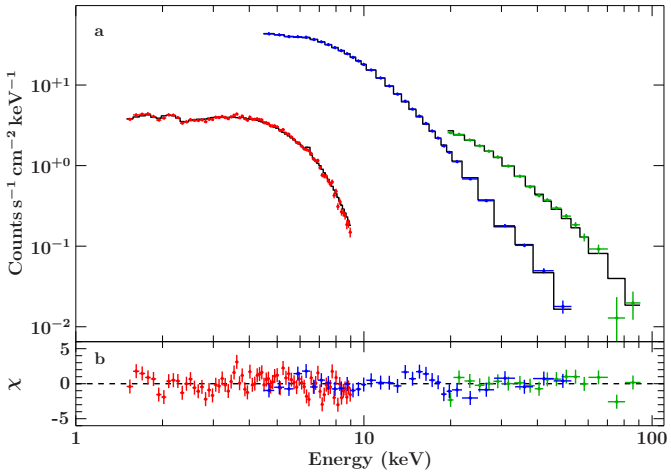


**Fig. 8. a)** Quasi-simultaneous 2007 *Swift* and RXTE spectra of GRO J1008−57 (*Swift*-XRT: red, RXTE-PCA: blue, RXTE-HEXTE: green). Spectral channels are grouped for display purposes. **b)** Residuals of a fit to the model given by Eq. (4).

where TBnew is a revised version of the absorption model of Wilms et al. (2000, see also Hanke et al. 2009), using the abundances of Wilms et al. (2000), and where BREMSS is a bremsstrahlung spectrum. The best-fit hydrogen column densities, $N_{\rm H}$, are consistent between both fits. They also agree

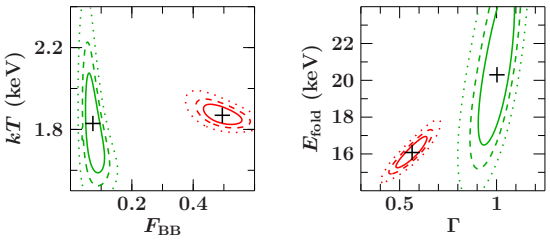


**Fig. 9.** Contour maps between several continuum parameters during the 2007 outburst. Each map is calculated from RXTE data near maximum luminosity (red; obs. 93032-03-02-00) and at the end of the outburst (green; obs. 93032-03-03-04). The solid line represents the $1\sigma$ contour, the dashed line $2\sigma$ and the dotted line $3\sigma$. The black-body flux, $F_{\rm BB}$, is given in units of $10^{-9}$ erg s$^{-1}$ cm$^{-2}$.

with the foreground absorption found in 21 cm surveys ($N_{\rm H} = 1.35^{+0.21}_{-0.09} \times 10^{22}$ cm$^{-2}$, Kalberla et al. 2005, and $N_{\rm H} = 1.51^{+0.38}_{-0.02} \times 10^{22}$ cm$^{-2}$, Dickey & Lockman 1990), as well as with the hydrogen column density of $1.49 \times 10^{22}$ cm$^{-2}$ obtained from the interstellar reddening of $E^{\rm is}(B-V) = 1.79(5)$ mag toward GRO J1008−57 (Riquelme et al. 2012, converted to $N_{\rm H}$ as outlined by Nowak et al. 2012).

### 4.2. Combined parameter evolution

A closer inspection of the best fits from both multi-satellite campaigns in Table 3 shows that most of the continuum parameters appear to be constant within their uncertainties. The only significant parameter change between both models is a change in the power-law flux by a factor of ∼2 because of the flux change of the source over the outburst.

Fitting all RXTE observations of the 2007 outburst with the basic model of Eq. (4) gives acceptable $\chi^2$-values for all observations. With the exception of the fluxes of the two continuum components, other spectral parameters appear to be constant within their error bars, although some scatter is still visible. Due to the lower sensitivity of RXTE compared with *Suzaku*, however, this scatter could be purely statistical in nature.

To illustrate the range of parameter variability, Fig. 9 shows contour maps between several continuum parameters calculated from RXTE data during maximum luminosity in 2007 (93032-03-02-00) and at the end of the 2007 outburst (93032-03-03-04). The contour map on the left demonstrates that the black body flux $F_{\rm BB}$ changes significantly over the outburst, while its temperature $kT_{\rm BB}$ can be described by the same values. Keeping this value fixed during both observations at a consistent value improves the uncertainty on the remaining parameters significantly. In particular, a contour map of Γ and $E_{\rm fold}$ reveals a strong correlation. Similar to the black-body temperature and the break energy, the folding energy seems to be consistent with a constant value during the outburst, while the photon index changes.

Inspection of the confidence maps reveals that the only spectral parameters for which significant changes are seen in individual spectral fits appear to be the power-law flux, $F_{\rm PL}$, the photon index Γ, and the black-body flux $F_{\rm BB}$. To constrain these parameters well and to reveal the evolution of the remaining parameters, all datasets available during the 2007 outburst (see Table 1) including the simultaneous *Swift* and *Suzaku* are fit simultaneously with the spectral continuum of Eq. (4) (and the Galactic ridge). In these fits the continuum parameters $N_{\rm H}$, $E_{\rm fold}$, and $kT$, and the flux calibration constant $C_{\rm HEXTE}$ are not allowed to vary between the different observations. The free parameters of the simultaneous fit are the fluxes of the spectral components, $F_{\rm PL}$ and $F_{\rm BB}$, the photon index, Γ, the iron line equivalent width $W$, and the PCA background scaling factor $b_{\rm PCA}$. Since the initial fit showed that the equivalent width of the iron line $W$ does not change significantly with source flux, in a final fit this parameter was also assumed to be the same for all observations.

**Table 4.** Source-flux-independent parameters, the iron line equivalent widths, the parameters of the Galactic ridge emission, and the HEXTE calibration constant as determined from the combined spectral analysis ($\chi^2_{\rm red}$/d.o.f. = 1.10/3651).

| | | |
|---|---|---|
| TBnew | $N_{\rm H}$ | $1.547^{+0.019}_{-0.023} \times 10^{22}$ cm$^{-2}$ |
| BBODY | $kT$ | $1.833^{+0.015}_{-0.017}$ keV |
| CUTOFFPL | $E_{\rm fold}$ | $15.92^{+0.24}_{-0.27}$ keV |
| Iron line | $W_{2005}$ | $65^{+10}_{-10}$ eV |
| | $W_{2007}$ | $27.9^{+2.4}_{-2.3}$ eV |
| | $W_{2011}$ | $83^{+5}_{-5}$ eV |
| Constants[a] | $c_{\rm HEXTE}$ | $0.859^{+0.009}_{-0.009}$ |
| | $c_{\rm XRT}$ | $0.806^{+0.009}_{-0.009}$ |
| | $c_{\rm XIS0}$ | $0.889^{+0.007}_{-0.007}$ |
| | $c_{\rm XIS1}$ | $0.936^{+0.007}_{-0.007}$ |
| | $c_{\rm XIS3}$ | $0.887^{+0.007}_{-0.007}$ |
| | $c_{\rm PIN}$ | $1.000^{+0.010}_{-0.010}$ |
| | $c_{\rm GSO}$ | $1.17^{+0.09}_{-0.09}$ |
| BREMSS[b] | $kT$ | $3.4^{+0.5}_{-0.5}$ keV |
| | $F_{\rm 3\text{-}10\,keV}$ | $4.25^{+0.20}_{-0.23} \times 10^{-12}$ erg s$^{-1}$ cm$^{-2}$ |
| Blended iron lines[b] | $E$ | $6.349^{+0.026}_{-0.031}$ keV |
| | $\sigma$ | $0.53^{+0.06}_{-0.05}$ keV |
| | $F$ | $2.39^{+0.17}_{-0.15} \times 10^{-4}$ photons s$^{-1}$ cm$^{-2}$ |

**Notes.** [(a)] detector calibration constants, $c$, are given relative to the RXTE-PCA. [(b)] Component belongs to the Galactic ridge emission and is applied to RXTE-PCA only (Eq. (5)).

The resulting model describes all 31 spectra of the 2007 outburst with an $\chi^2_{\rm red} = 1.12$ for 2623 d.o.f.. Adding all RXTE-data of the 2005 and 2011 April outbursts to check for possible hysteresis effects and refitting shows that the simplified model still gives a good description of all data if the equivalent width of the iron line is allowed to change between different outbursts (but remaining constant during each outburst). With $N_{\rm H} = 1.6 \times 10^{22}$ cm$^{-2}$, the soft X-ray absorption is too low to be constrained by PCA-data only. For this reason, changes of $N_{\rm H}$ between the outbursts cannot be detected in the PCA data and the column density is held fixed for all outbursts. The best-fit $\chi^2$ for this fit of 68 spectra is $\chi^2_{\rm red} = 1.10$ for 3639 d.o.f.. Finally, to constrain the Galactic ridge emission further, the summed spectrum of the quiescent state in 1996/1997 was added to the simultaneous fit.

The final combined analysis of all 2005, 2007, and 2011 April data (compare Table 1) results in a remarkable fit with an $\chi^2_{\rm red} \approx 1.10$ for 3651 d.o.f.. The flux-independent parameters, $N_{\rm H}$, $E_{\rm fold}$, and $kT$, the outburst dependent parameters (iron line equivalent widths), the Galactic ridge parameters, and the calibration constant are presented in Table 4.

Thanks to the combined fits of all available data, the uncertainties of all parameters can be reduced significantly by comparing Table 4 with Table 3. This is not only seen for the flux-independent parameters, but also for the continuum parameters allowed to vary for each observation, especially for those at low source luminosity, where only four parameters are required to describe the source spectrum. In addition to an instrumental parameter, the PCA background factor, $b_{\rm PCA}$, the three physical parameters describing the evolution of the spectral continuum are the photon index Γ, the black body flux, $F_{\rm BB}$, and the

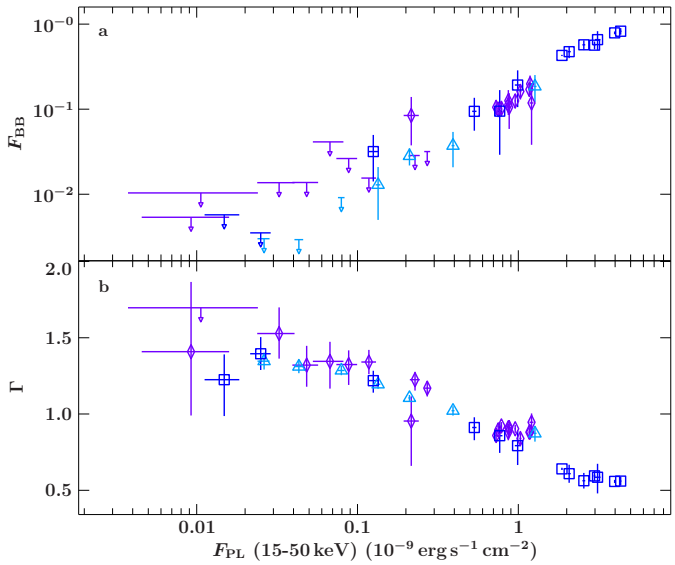


**Fig. 10.** **a)** Black-body flux, $F_{BB}$ in $10^{-9}$ erg s$^{-1}$ cm$^{-2}$, and **b)** photon index, Γ, both strongly correlate with the power-law flux, $F_{PL}$. Light-blue triangles and dark-blue squares represent data from the decays of the 2005 and 2007 outbursts, respectively, purple diamonds are from the rise of the 2011 April outburst (Table 1 and Fig. 1).

power law flux, $F_{PL}$. As shown in Fig. 10, the three parameters are strongly correlated: the photon index decreases with $\log F_{PL}$, i.e., the source hardens with luminosity, and the black-body flux increases linearly with powerlaw flux. Note that the trend from the rise of the 2011 outburst (purple diamonds) is equal to the trends of the declines of both outbursts in 2005 and 2007. Thus, the spectral shape does not depend on the sign of the time derivative of the flux.

The relationships shown in Fig. 10 can be used to reduce the number of parameters needed to describe the spectrum of GRO J1008−57 to one, $F_{PL}$, if the flux independent parameters are fixed to the values listed in Table 4. A fit to the data shown in Fig. 10 gives the following empirical relationships:

$$\Gamma = a + b \ln\left(\frac{F_{PL}}{10^{-9}\,\mathrm{erg\,s^{-1}\,cm^{-2}}}\right) \quad (6)$$

and

$$\frac{F_{BB}}{10^{-9}\,\mathrm{erg\,s^{-1}\,cm^{-2}}} = c + d\,\frac{F_{PL}}{10^{-9}\,\mathrm{erg\,s^{-1}\,cm^{-2}}}, \quad (7)$$

with $a = 0.834(10)$, $b = -0.184(8)$ and $c = -0.019(7)$, $d = 0.191(9)$ ($\chi^2_{red} = 1.82$, 38 d.o.f. and $\chi^2_{red} = 1.09$, 24 d.o.f., respectively). Using the $c$ parameter of the straight line describing the black-body flux, one finds that the black body starts to contribute significantly once the power law reached a 15–50 keV flux of $10(4) \times 10^{-11}$ erg s$^{-1}$ cm$^{-2}$. Integrating the modelflux between 0.01−100 keV, this corresponds to a total luminosity of $13(5) \times 10^{35}$ erg s$^{-1}$ assuming a distance of 5.8 kpc (Riquelme et al. 2012).

In both fits, the data points resulting from the *Suzaku*-spectra were ignored, since they differ significantly from the best fit to the correlations. This difference is due to energy calibration differences between RXTE and *Suzaku*, which lead to a slight change in the fitted power-law photon index Γ of $\Delta\Gamma \sim 0.1$. Such differences in photon index are typical between missions. See, e.g., Kirsch et al. 2005, who found differences up to $\Delta\Gamma = 0.2$ between different missions in their analysis of the Crab pulsar and nebula.

**Table 5.** Parameters of the possible cyclotron resonant scattering feature around 88 keV.

| Parameter | This work | Shrader et al. (1999) | Unit |
|---|---|---|---|
| $E_0$ | $86^{+7}_{-5}$ | $88^{+2.4}_{-2.4}$ | keV |
| $W$ | $8^{+6}_{-4}$ | 20 (fixed) | keV |
| $\tau$ | 2.3 (fixed) | $2.3^{+6}_{-6}$ | |

**Notes.** See text for a more detailed discussion.

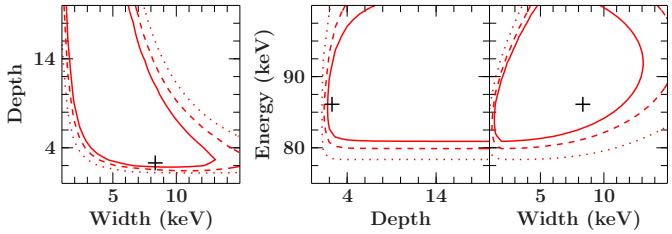


**Fig. 11.** Contour maps between the CYCLABS-parameters used to model the absorption above 75 keV. The solid line represents the $1\sigma$ contour, the dashed line $2\sigma$, and the dotted line $3\sigma$.

### 4.3. Cyclotron resonant scattering feature

As discussed in Sect. 4.1, a possible absorption-like feature above 75 keV is visible in the *Suzaku*-GSO and RXTE-HEXTE spectra (Figs. 7 and 8, respectively). Initial attempts to fit this feature were unsuccessful because of its rather low significance and strong correlations between the continuum parameters and the line parameters. The flux dependency of the continuum parameters (Eqs. (6) and (7)) and the large number of flux-independent spectral components (Table 4) significantly reduce the number of continuum parameters. To describe the line, the continuum model of Eq. (4) was modified with a multiplicative cyclotron line model of the form

$$\mathtt{CYCLABS}(E) = \exp\left(-\frac{\tau(WE/E_{cyc})^2}{(E-E_{cyc})^2 + W^2}\right), \quad (8)$$

where $E_{cyc}$ is the centroid energy, $W$ the width, and $\tau$ the optical depth of the cyclotron line. Performing a fit to the simultaneous *Suzaku* and RXTE spectrum measured in 2007 results in a satisfactory description of the cyclotron line. The best-fit parameters together with the historic values determined using CGRO-OSSE data are shown in Table 5. The depth is fixed to the value found by Shrader et al. (1999) since the signal-to-noise ratio in the line core is close to unity, allowing the modeled depth to take any arbitrary value. Although the remaining parameters are consistent with previous results, the data quality at these high energies does not allow one to constrain any parameters well, however. In addition, the $\chi^2$-contours of the line parameters plotted in Fig. 11 reveal strong correlations. The centroid energy of the absorption feature is consistent with nearly any value above 75 keV. Even a combined fit of all RXTE data with the CYCLABS model added does not improve the fits, nor does it constrain the parameters better. Despite the large number of observations presented here, it is therefore difficult to distinguish between a cyclotron resonant scattering feature and a modification of the shape of the high-energy cutoff away from a pure exponential cutoff at these energies.

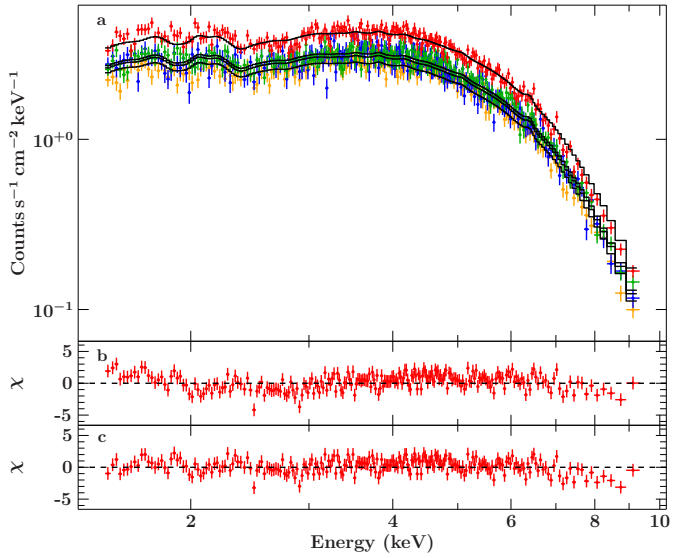


**Fig. 12. a)** Best fit of the four *Swift*-XRT spectra of the 2011 December outburst. **b)** Combined residuals after applying the same model to the data as used in the previous analysis (see text). The only three free spectral parameters are the power-law flux, the absorption column density, and the Fe K$\alpha$ equivalent width. **c)** Combined residuals after applying a partial coverer model (see text and Eq. (9)).

## 5. 2011 December outburst of GRO J1008−57

In 2011 December, GRO J1008−57 underwent an even stronger outburst than the outburst of 2007 we analyzed in the previous sections. The peak flux in *Swift*-BAT of ∼320 mCrab was reached exactly at the expected date around MJD 55 913 predicted by the orbital ephemeris from Sect. 3.

*Swift* ToO observations obtained by the authors as a result of this prediction are listed in Table 1. No other X-ray data of sufficient quality of this outburst are available in the archive and, therefore, the high-energy part of the spectrum above 10 keV is not available for analysis. The measurements made during this outburst, which did not enter the analysis in the previous section, provide a good test for the overall reliability of the simple continuum model behavior found from the earlier outbursts. Fixing the flux-independent continuum parameters and $N_{\rm H}$-value to the values listed in Table 4, and expressing $\Gamma$ and $F_{\rm BB}$ as a function of power-law flux through Eqs. (6) and (7), the two free fit parameters are the power-law flux and the combined iron line equivalent width.

An initial combined fit of all four *Swift*-XRT spectra yields an unacceptable fit of $\chi^2_{\rm red} = 3.7$. This result is due to residuals below 4 keV, which is strong evidence for a change in the absorption column density. Allowing this parameter to vary results in a reasonable fit of $\chi^2_{\rm red} = 1.23$ for 934 d.o.f.. There are slight deviations from a perfect fit left, however (Fig. 12b). If a partial coverer model of the form

$$F_{\rm ph,partial} = ((1-f)\times \texttt{TBnew}(N_{\rm H,1}) + f\times \texttt{TBnew}(N_{\rm H,2}))\, F_{\rm ph,model}(E), \quad (9)$$

where $f$ is the covering factor, is applied to the model, the quality of the fit is slightly increased ($\chi^2_{\rm red} = 1.12$ for 932 d.o.f.). Note, however, that the spectra can also be described by adding a secondary black-body component with a temperature of 0.25 keV. This latter approach results in an even better description of the data ($\chi^2_{\rm red} = 1.07$ for 922 d.o.f.). The parameters of the two possible models are shown in Table 6 and the spectra with the secondary black-body model applied are shown in Fig. 12. Data

**Table 6.** Spectral parameters of a fit to the *Swift*-XRT spectra of the 2011 December outburst using a partial coverer model ($\chi^2_{\rm red}$ = 1.12, 932 d.o.f.) and a secondary black-body component ($\chi^2_{\rm red}$ = 1.07, 929 d.o.f.).

| Component | | Part. cov. | 2nd black body | Unit |
|---|---|---|---|---|
| TBnew | $N_{\rm H,1}$ | $1.45^{+0.20}_{-0.33}$ | $2.99^{+0.20}_{-0.19}$ | $10^{22}$ cm$^{-2}$ |
| | $N_{\rm H,2}$ | $8.9^{+3.4}_{-2.7}$ | – | $10^{22}$ cm$^{-2}$ |
| | $f$ | $0.27^{+0.13}_{-0.07}$ | – | |
| BBODY[a] | $kT$ | – | $0.244^{+0.017}_{-0.019}$ | keV |
| | $F_{\rm BB,1}$ | – | $0.85^{+0.21}_{-0.16}$ | $10^{-9}$ erg s$^{-1}$ cm$^{-2}$ |
| | $F_{\rm BB,2}$ | – | $0.58^{+0.16}_{-0.14}$ | $10^{-9}$ erg s$^{-1}$ cm$^{-2}$ |
| | $F_{\rm BB,3}$ | – | $0.53^{+0.16}_{-0.14}$ | $10^{-9}$ erg s$^{-1}$ cm$^{-2}$ |
| | $F_{\rm BB,4}$ | – | $0.35^{+0.13}_{-0.11}$ | $10^{-9}$ erg s$^{-1}$ cm$^{-2}$ |
| PL[a] | $F_{\rm PL,1}$ | $4.65^{+0.10}_{-0.08}$ | $4.61^{+0.08}_{-0.08}$ | $10^{-9}$ erg s$^{-1}$ cm$^{-2}$ |
| | $F_{\rm PL,2}$ | $3.52^{+0.08}_{-0.08}$ | $3.54^{+0.06}_{-0.06}$ | $10^{-9}$ erg s$^{-1}$ cm$^{-2}$ |
| | $F_{\rm PL,3}$ | $3.33^{+0.08}_{-0.08}$ | $3.33^{+0.08}_{-0.08}$ | $10^{-9}$ erg s$^{-1}$ cm$^{-2}$ |
| | $F_{\rm PL,4}$ | $2.87^{+0.06}_{-0.06}$ | $2.93^{+0.06}_{-0.06}$ | $10^{-9}$ erg s$^{-1}$ cm$^{-2}$ |
| Iron line | $W$ | $17^{+10}_{-10}$ | $16^{+10}_{-10}$ | eV |

**Notes.** [(a)] $F_{{\rm PL},i}$ is the 15–50 keV flux and $F_{{\rm BB,i}}$ is the bolometric black body flux of the $i$th *Swift* observation of 2011 December (Table 1), scaled to the PCA via the detector calibration constant $c_{\rm XRT}$ (Table 3).

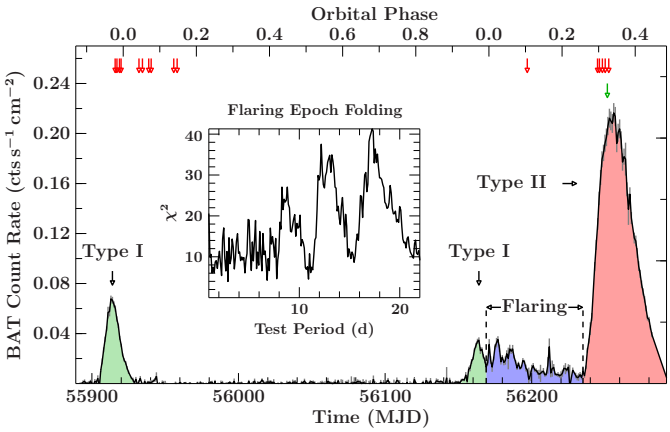


**Fig. 13.** *Swift*-BAT light curve showing the 2011 December and the 2012 August outburst, which occurred as predicted by the orbital ephemeris (green region), and the unexpected flaring activity after this outburst (blue region) followed by a giant type II outburst at an orbital phase of nearly 0.3 (red region). Times of observation by *Swift* (red) and *Suzaku* (green) are shown as arrows on top (compare Table 1). The inset shows the epoch-folding result of the flaring part of the light curve.

from the outbursts of GRO J1008−57 in 2012 show that there is indeed an additional soft excess instead of a partial covering material (see Sects. 6 and 7 below).

Twelve days after the last *Swift* pointing during the outburst, on MJD 55 932, *Swift* started to observe GRO J1008−57 again. Until MJD 55 958, six additional observations were made (see Table 1). Even though the *Swift*-BAT did not detect the source (Fig. 13), *Swift*-XRT images clearly reveal an X-ray source at the position of GRO J1008−57, indicating that the neutron star was still accreting. Although the extracted *Swift*-XRT spectra have a few hundred photons only, by performing a combined fit of all six spectra and using the same model as described above (without need of a partial coverer model or secondary black body), the data can be well described with an $\chi^2_{\rm red} = 1.05$ for 65 d.o.f.

**Table 7.** Spectral parameters of a fit to the *Swift*-XRT spectra after the 2011 December outburst ($\chi^2_{\rm red}$ = 1.05, 65 d.o.f.).

| | | |
|---|---|---|
| TBnew | $N_{\rm H}$ | $4.3^{+0.7}_{-0.6} \times 10^{22}$ cm$^{-2}$ |
| PL[a] | $F_{\rm PL,1}$ | $5.9^{+1.8}_{-1.6} \times 10^{-12}$ erg s$^{-1}$ cm$^{-2}$ |
| | $F_{\rm PL,2}$ | $7.8^{+1.9}_{-1.7} \times 10^{-12}$ erg s$^{-1}$ cm$^{-2}$ |
| | $F_{\rm PL,3}$ | $4.0^{+1.4}_{-1.2} \times 10^{-12}$ erg s$^{-1}$ cm$^{-2}$ |
| | $F_{\rm PL,4}$ | $2.9^{+0.9}_{-0.8} \times 10^{-12}$ erg s$^{-1}$ cm$^{-2}$ |
| | $F_{\rm PL,5}$ | $0.28^{+0.26}_{-0.19} \times 10^{-12}$ erg s$^{-1}$ cm$^{-2}$ |
| | $F_{\rm PL,6}$ | $1.8^{+0.8}_{-0.7} \times 10^{-12}$ erg s$^{-1}$ cm$^{-2}$ |

**Notes.** [(a)] $F_{{\rm PL},i}$ is the 15–50 keV flux of the $i$th *Swift* observation after 2011 December (Table 1), scaled to the PCA via the detector calibration constant $c_{\rm XRT}$ (Table 3).

**Table 8.** Spectral parameters of a fit to the *Swift*-XRT spectrum during the flaring activity after the 2012 August outburst ($\chi^2_{\rm red}$ = 0.97, 117 d.o.f.).

| | | |
|---|---|---|
| TBnew | $N_{\rm H}$ | $2.04^{+0.23}_{-0.22} \times 10^{22}$ cm$^{-2}$ |
| PL[a] | $F_{\rm PL}$ | $1.81^{+0.11}_{-0.11} \times 10^{-9}$ erg s$^{-1}$ cm$^{-2}$ |
| Iron line | $W$ | $110^{+90}_{-90}$ eV |

**Notes.** [(a)] $F_{\rm PL}$ is the 15–50 keV power law flux, scaled to the PCA via the detector calibration constant $c_{\rm XRT}$ (Table 3).

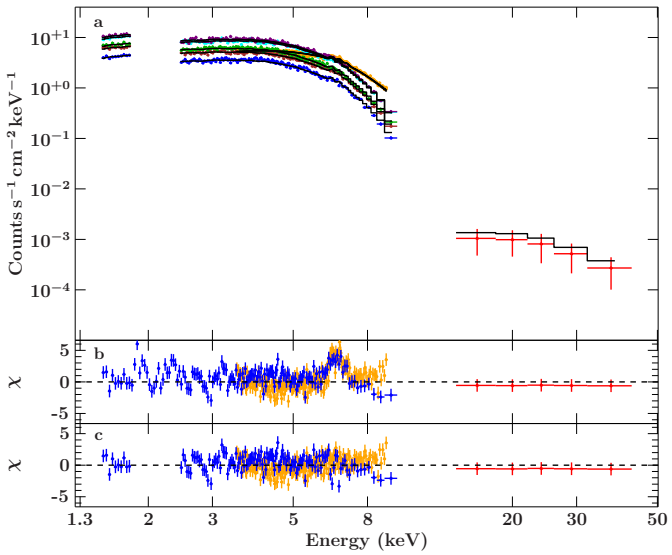


**Fig. 14. a)** Five *Swift*-XRT (blue), *Swift*-BAT (red) and *Suzaku*-XIS spectra of the type II 2012 November outburst of GRO J1008−57. Spectral channels are rebinned for display purposes. **b)** Combined residuals after applying the same model to the data as used in the previous analysis, including the secondary black body (see text). **c)** Best-fit combined residuals after excluding calibration features between 1.7 and 2.4 keV and adding three narrow Fe lines at 6.4, 6.67 keV, and 7 keV (compare Fig. 15).

The final parameters are listed in Table 7. The hydrogen column density is slightly higher than the value during the main outburst in 2011 December. This can be explained by the position of the neutron star on the orbit, which is behind the companion as seen from Earth. Here, the line of sight crosses a much larger region within the system (see Fig. 2), and thus increased absorption caused by the normal orbital modulation of $N_{\rm H}$ is expected (see Hanke et al. 2010 and Hanke 2011 for a discussion of similar behavior in the HMXBs Cygnus X-1 and LMC X-1).

To conclude, the model of GRO J1008−57 found using the earlier data analyzed in the previous sections works for other outbursts as well. GRO J1008−57's behavior is therefore independent of the outburst history.

## 6. Predicting the unpredictable: the 2012 November type II outburst of GRO J1008−57

Although GRO J1008−57 seems to be predictable for the occurrence of outbursts and the spectral shape, an unexpected and unpredictable behavior occurred immediately after the outburst in 2012 August, which itself occurred at the expected time. Instead of fading into quiescence, the outburst decay lasted several weeks, during which several flares were detected (see Fig. 13). An epoch folding (Leahy et al. 1983) of the flaring activity in the light curve reveals significant variability on timescales on the order of 10 d and above (see Fig. 13, inset).

*Swift* observed GRO J1008−57 during the flaring activity on 2012 September 26/27. Because of the low flux (∼1.14 × $10^{-9}$ erg s$^{-1}$ cm$^{-2}$), the XRT data were grouped to achieve a minimum signal-to-noise ratio of 5. The same model as used for the previous outbursts was then applied to the data, which resulted in an good fit ($\chi^2_{\rm red}$ = 0.97, 117 d.o.f.). The corresponding spectral parameters are listed in Table 8. Although the best-fit iron line equivalent width is much larger than during previous outbursts, the lower confidence limit still agrees with the value during the 2011 December outburst.

After the flares, on 2012 November 13, the BAT instrument onboard *Swift* was triggered by a sudden flux increase of GRO J1008−57 (Krimm et al. 2012). The flux reached 1 Crab within a few days, indicating another outburst of the source. This flux was about three times higher than the strongest outburst detected previously, except for the discovery outburst (Shrader et al. 1999), and nearly one order of magnitude higher than the mean maximal flux over all outbursts detected by ASM and BAT (Fig. 1). According to the orbital parameters listed in Table 2, the unexpected outburst occured close to orbital phase 0.3 (see also Nakajima et al. 2012). This unusual behavior is typical for type II outbursts, which have been seen in many other Be X-ray binaries such as A0535+26 (Caballero et al. 2012) or EXO 2030+375 (Klochkov et al. 2008).

The spectra of GRO J1008−57 as observed by *Swift*-XRT, *Swift*-BAT and *Suzaku*-XIS are shown in Fig. 14. The model applied to the data is the same as used for the previous outbursts. The *Swift* spectra agree well with this model after excluding calibration features at ∼1.8 keV and ∼2.2 keV, accounting for the calibration of the Si K edge and the Au M edge, respectively (Godet et al. 2007; Hurkett et al. 2008). The BAT-spectrum was rebinned to a signal-to-noise ratio of 1.5 in the energy range of 14 to 40 keV. Because of the high flux level of the source, data from *Suzaku*-XIS were extracted, avoiding regions with more than 2% pile-up fraction.

An initial fit reveals residuals, which are most prominent in *Suzaku*-XIS, and are of similar shape to the residuals seen in the 2011 December outburst (compare Fig. 12). A partial covering model is not able to fit the residual structure. Using a secondary black-body component results in a better description of the data. Its temperature of around 0.39 keV is similar to the value found in the 2011 December data. A complex structure below 3.5 keV remains in the residuals of *Suzaku*-XIS, which is not present

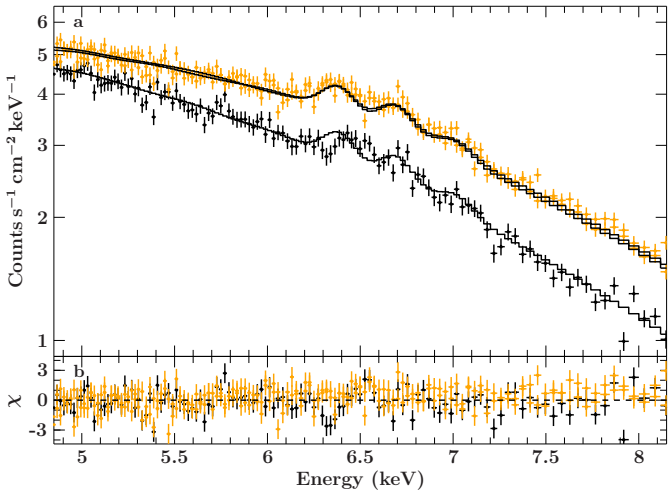


**Fig. 15. a)** Iron line complex in *Suzaku*-XIS (orange: XIS0/3, black: XIS1). The neutral, hydrogen- and helium-like emission lines are clearly visible as well as the shift in the line centroid energies between XIS1 and XIS0/3. **b)** Residuals of the fit (see text).

in *Swift*-XRT data. Since the overall continuum shape is modeled successfully, XIS-data below 3.5 keV were removed from the analysis for the time being.

In addition to the continuum model, an unresolved residual structure consistent with the presence of three narrow Fe emission lines at 6.4, 6.67 and 7 keV is visible in the spectra (see Fig. 15), corresponding to neutral Fe K$\alpha$ fluorescence and recombination lines from He-like and H-like iron. The centroid energies of the fluorescent lines, which were fixed relative to neutral iron emission at 6.4 keV, are shifted by ∼+0.1 keV between the front illuminated XIS1 and the back-illuminated XIS0 and XIS3. This is probably due to calibration problems, such as a gain shift. To ensure that the line parameters are not affected by this energy shift, data from XIS1 were excluded from the final fit. With these modifications, we obtained a good description of the data ($\chi^2_{\rm red}$ = 1.08, 2582 d.o.f.). The equivalent widths of these lines together with the fluxes, the secondary black-body parameters, and the absorption column density are listed in Table 9.

During the 2012 November outburst the hydrogen column density was similar to the preceding flaring activity and the 2007 December outburst, which itself agrees with the galactic hydrogen column density (Tables 8 and 3). As the observations during and after the 2011 December outburst show, the column density might still change between outbursts (Tables 6 and 7). The extreme flux increase during the 2012 giant outburst requires a large amount of material. This is in contrast to the relatively low hydrogen column density. The ionized iron in the system indicates significant amounts of almost fully ionized plasma, however, probably due to photoionization caused by the very luminous neutron star, which would not be detected in absorption by X-ray spectroscopy. This would effectively cause a decrease of the measured neutral hydrogen column density down to the galactic value.

Performing a pulse period analysis of the five *Swift*-XRT lightcurves during the giant outburst, which were corrected for binary motion using the parameters listed in Table 2, reveals a significantly faster rotation period of the neutron star of $P$ = 93.6483(7) s and a spin-up of $\dot{P} = -0.60(4) \times 10^{-7}$ s s$^{-1}$.

**Table 9.** Spectral parameters of a fit to the five *Swift*-XRT, *Swift*-BAT, and *Suzaku*-XIS spectra of the giant 2012 November outburst ($\chi^2_{\rm red}$ = 1.08, 2582 d.o.f.).

| | | |
|---|---|---|
| TBnew | $N_{\rm H}$ | $1.86^{+0.24}_{-0.25} \times 10^{22}$ cm$^{-2}$ |
| PL[a] | $F_{\rm PL,1}$ | $9.82^{+0.11}_{-0.11} \times 10^{-9}$ erg s$^{-1}$ cm$^{-2}$ |
| | $F_{\rm PL,2}$ | $10.46^{+0.13}_{-0.11} \times 10^{-9}$ erg s$^{-1}$ cm$^{-2}$ |
| | $F_{\rm PL,3}$ | $11.55^{+0.13}_{-0.13} \times 10^{-9}$ erg s$^{-1}$ cm$^{-2}$ |
| | $F_{\rm PL,4}$ | $14.69^{+0.14}_{-0.14} \times 10^{-9}$ erg s$^{-1}$ cm$^{-2}$ |
| | $F_{\rm PL,5}$ | $14.31^{+0.16}_{-0.16} \times 10^{-9}$ erg s$^{-1}$ cm$^{-2}$ |
| | $F_{\rm PL,Suz.}$ | $11.71^{+0.08}_{-0.08} \times 10^{-9}$ erg s$^{-1}$ cm$^{-2}$ |
| BBODY[a] | $kT$ | $0.390^{+0.017}_{-0.014}$ keV |
| | $F_{\rm BB,1}$ | $0.541^{+0.042}_{-0.042} \times 10^{-9}$ erg s$^{-1}$ cm$^{-2}$ |
| | $F_{\rm BB,2}$ | $0.591^{+0.042}_{-0.042} \times 10^{-9}$ erg s$^{-1}$ cm$^{-2}$ |
| | $F_{\rm BB,3}$ | $0.620^{+0.045}_{-0.045} \times 10^{-9}$ erg s$^{-1}$ cm$^{-2}$ |
| | $F_{\rm BB,4}$ | $0.779^{+0.045}_{-0.045} \times 10^{-9}$ erg s$^{-1}$ cm$^{-2}$ |
| | $F_{\rm BB,5}$ | $0.88^{+0.06}_{-0.06} \times 10^{-9}$ erg s$^{-1}$ cm$^{-2}$ |
| | $F_{\rm BB,Suz.}$ | $0.64^{+0.32}_{-0.32} \times 10^{-9}$ erg s$^{-1}$ cm$^{-2}$ |
| Iron line | $W_{\rm neutral}$ | $30^{+4}_{-4}$ eV |
| | $W_{\rm He\text{-}like}$ | $32^{+5}_{-5}$ eV |
| | $W_{\rm H\text{-}like}$ | $17^{+5}_{-5}$ eV |
| Constants | $c_{\rm XIS0}$ | $0.787^{+0.006}_{-0.006}$ |

**Notes.** [(a)] $F_{{\rm PL},i}$ is the 15–50 keV flux and $F_{\rm BB,i}$ is the bolometric flux of the secondary black body of the $i$th *Swift* observation of 2012 November as listed in Table 1, scaled to the PCA via the detector calibration constant $c_{\rm XRT}$ and $c_{\rm XIS3}$ (Table 3). The calibration constant $c_{\rm XIS0}$ had to be refitted. $F_{\rm PL,Suz.}$ and $F_{\rm BB,Suz.}$ are the corresponding fluxes obtained by the *Suzaku* observation.

## 7. Conclusions

In the previous sections, all available RXTE observations of GRO J1008−57 including three outbursts in 2005, 2007, and 2011 April as well as an observation campaign during source quiescence in 1996/1997 were analyzed. In addition to these data *Swift* and *Suzaku* observations during the 2007 outburst were combined with the RXTE analysis, and *Swift* observations of the 2011 December and "giant" 2012 November outbursts were compared with the spectral results of the previous outbursts.

By performing a detailed pulse arrival-time analysis, the orbital period of the binary and the time of periastron passage were improved (see Table 2). In addition, a slight nonlinear spin-up of the neutron star in the order of $10^{-14}$ s s$^{-2}$ was detected during high luminosity of the 2007 outburst. This pulse ephemeris implies a spin-up rate of $-2 \times 10^{-8}$ s s$^{-1}$ at maximum luminosity around MJD 54 428. During the giant 2012 outburst, the measured value of $-6 \times 10^{-8}$ s s$^{-1}$ is three times higher than the 2007 value. This difference is consistent with theory, where the spin-up rate $\dot{P}$ is connected to the luminosity $L$ via (Ghosh & Lamb 1979)

$$-\dot{P} \propto L^{\alpha}, \tag{10}$$

with $\alpha$ = 1 for wind- and $\alpha$ = 6/7 for disk-accretion. The maximum luminosity during the giant 2012 outburst was about three times higher than during the 2007 outburst.

The evolution of the period over the decades as shown in Fig. 16 reveals, however, that the long-term evolution is dominated by a spin-down in the order of $2 \times 10^{-10}$ s s$^{-1}$.

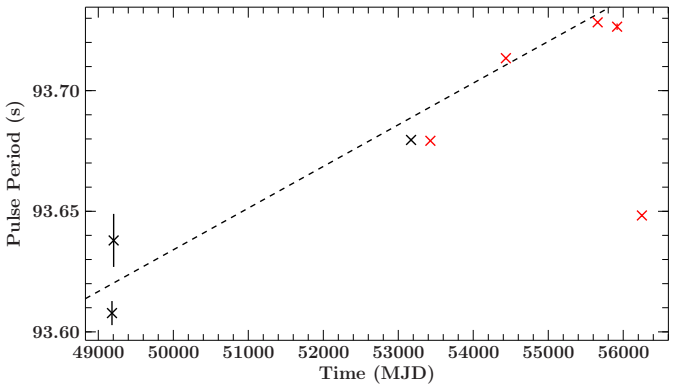


**Fig. 16.** Spin period evolution of GRO J1008−57 since its discovery. Black: historic data taken from Stollberg et al. (1993), Shrader et al. (1999), and Coe et al. (2007). Red: results of this work. The latest period measurement was taken during the "giant" 2012 outburst. To guide the eye, the dashed line shows a spin-down of $2 \times 10^{-10}$ s s$^{-1}$.

A similar long-term behavior was detected in A0535+26 by Camero-Arranz et al. (2012, see also Bildsten et al. 1997). Such a long-term spin-down might be evidence for the "propeller" regime, where matter near the neutron star is expelled, removing angular momentum and causing the neutron star to spin down (Illarionov & Sunyaev 1975; Frank et al. 1992; Bildsten et al. 1997). In the propeller regime, the magnitude of the spin-down is

$$\dot{P} = \frac{10\pi\mu^2}{GM^2R^2} \quad \text{where} \quad \mu = \frac{1}{2}BR^3, \tag{11}$$

where $B$ is the magnetic field strength on the polar caps of the neutron star and where all other symbols have their usual meaning. Assuming a mass $M = 1.4\,M_\odot$ and a radius $R = 10$ km of the neutron star and $\dot{P}$ as estimated from Fig. 16, the surface magnetic field strength of GRO J1008−57 is $B \sim 2.6{\times}10^{12}$ G. This is a reasonable value for an accreting neutron star in an HMXB and implies a fundamental CRSF at 30 keV in the X-ray spectrum. Note, however, that since the spin-up phases during outbursts lead to a lower observed long-term spin-down, the derived magnetic field strength without taking this spin-up into account is most likely a lower limit.

Using the precise orbital solution allows a detailed study of the connection of outbursts with the orbit. For GRO J1008−57 all outbursts detected in RXTE-ASM and *Swift*-BAT until 2012 May are clearly connected to the periastron passage, with the peak flux occurring close to periastron (Fig. 6). This behavior is in line with results from a recent study of Be outburst behavior by Okazaki et al. (2013). These authors showed that type I outbursts occur close to periastron in Be systems, where the neutron star can accrete from a tidally truncated Be-disk. According to Okazaki et al. (2013), type I outbursts occur regularly only in systems with high eccentricity ($\gtrsim$0.6), where the Be disk is truncated close to the critical Roche Lobe radius. The regularity of type I outbursts is increased in systems with long orbital periods, where the disturbance of the Be-disk is minimized. Both conditions are fulfilled in GRO J1008−57, for which Okazaki & Negueruela (2001) calculated the disk of the donor to be truncated at the 7:1 or 8:1 resonance and concluded that this system should show regular type I outbursts. Another prediction is that type II "giant" outbursts can happen if there is a misalignment between the Be-disk and the orbital plane (Okazaki et al. 2013). These outbursts would then be triggered, e.g., by increased activity of the donor star as seen, for example, in A0535+26 (e.g., Yan et al. 2012). There are indications that such a misalignment is also present in GRO J1008−57, since the type I outburst maximum occurs slightly before periastron (Fig. 6). Note that another Be source, 2S1845−024, shows similar behavior (Finger et al. 1999), although here the regular type I outbursts occur slightly after periastron.

Between the ordinary type I outburst in August 2012 and the giant type II outburst several flares were detected in *Swift*-BAT (see Fig. 13). An epoch folding (Leahy et al. 1983) of that time range revealed oscillations in the order of ∼10 d (see inset of Fig. 13). The origin of these oscillations is unknown.

As shown in Sect. 4.1, the spectrum of GRO J1008−57 can be well described by a cut-off power law with an additional black-body component, with some spectral parameters being independent of flux and outburst (Table 8). The physical reason might be found in the unique properties of the neutron star in GRO J1008−57, such as its magnetic field strength, mass and radius. Without a working physical model describing the spectra of accreting neutrons stars it is not possible to investigate this aspect in more detail, however. Nevertheless, GRO J1008−57 is an ideal candidate to test future physical models, which are still in development (see Becker & Wolff 2007, and references therein). For a distance of 5.8 kpc and a neutron star with 10 km radius, the maximum observed source flux during the 2007 December outburst corresponds to an emission area of around 1.5% of the neutron star's surface. Even during the giant 2012 November outburst the derived area fraction was only 5%. These values agree well with estimates of the hot-spot size at the magnetic poles (e.g., Gnedin & Sunyaev 1973; Ostriker & Davidson 1973).

Similar correlations as the one discovered between the photon index $\Gamma$ and the black-body flux $F_{\rm BB}$ with the power-law flux $F_{\rm PL}$ (Fig. 10) have been seen in other Be X-ray binaries as well, as reported in Reig & Nespoli (2013). These authors analyzed the PCA-data of the 2007 outburst of GRO J1008−57 and found a similar correlation between the power-law and the source luminosity. In addition, they discovered a correlation between the folding energy and the photon index. Taking the HEXTE-data into account, Fig. 9 shows, however, that the data are consistent with a constant folding energy.

The spectrum of GRO J1008−57 hardens with increasing luminosity. Recent theoretical work by Becker et al. (2012) describes several spectral states depending on the source luminosity, where sources with luminosities below the Eddington limit are expected to show this kind of correlation. Assuming a source distance of 5.8 kpc (Riquelme et al. 2012) and using the maximum flux values given in Table 3, the peak luminosity (0.01−100 keV) of GRO J1008−57 is around $3 \times 10^{37}$ erg s$^{-1}$. This value is close to the critical luminosity reported by Becker et al. (2012), which scales like $L_{\rm crit} \sim 1.5 \times 10^{37} B_{12}^{16/15}$. Thus, GRO J1008−57 is very likely to be a subcritical accretor during type I outbursts.

The most remarkable result of the analysis of the giant type II outburst of GRO J1008−57 is that the spectral model found for type I outbursts (Eq. (4) with flux-independent parameters from Table 3 and flux correlations from Eqs. (6) and (7)) is also able to describe the type II hard X-ray (>10 keV) spectrum. The main contribution in that energy range is the power-law component, which emerges from inverse Compton effects in the accretion column far above the neutron star's surface. To describe the soft X-ray spectrum, however, an additional soft component is needed (the second black body). This suggests a change in the accretion mechanisms near the neutron star's surface, where Comptonization processes take place and

shocks may form as described in Becker et al. (2012). Following the findings of these authors, the derived 0.01−100 keV luminosity of GRO J1008−57 during the giant outburst is close to $10^{38}$ erg s$^{-1}$, which indicates that the neutron star is accreting supercritically. Thus, the spectral change in the soft X-rays might be generated by supercritical accretion. A similar black-body component had to be introduced for the 2011 December outburst (see Table 6). Compared with the additional soft component of the 2012 giant outburst, its bolometric flux contributes much less. That indicates that the source was close to or in the transition from the sub- to the supercritial accretion regime during the 2011 December outburst. These findings agree with and confirm the state changes in neutron star Be X-ray binaries as proposed by Reig & Nespoli (2013), who found a softening of the spectrum close to or above the critical luminosity.

Neutral material in the vicinity of the neutron star is believed to be the origin of observed fluorescence lines, e.g., the 6.4 keV iron K$\alpha$ line. For $N_{\rm H} \lesssim 10^{23}$ cm$^{-2}$, self-absorption is not important and the iron line equivalent width and the hydrogen column density scale roughly linearly (Eikmann 2012). The generally low observed equivalent widths indicate that the fluorescence line originates in the absorbing material. In most observations, $N_{\rm H}$ agrees with the interstellar value, although some intrinsic absorption cannot be ruled out. During the 2012 August outburst, the best-fit Fe K$\alpha$ equivalent width is much larger (although with large uncertainties). This larger equivalent width could be due to the addition of a line from reflection from an enhanced Be disk, for instance. If the X-rays are reflected by material, the equivalent width increases significantly to a factor of 100.

The data analyzed within this paper cannot confirm the claimed cyclotron line at 88 keV by Shrader et al. (1999, see Sect. 4.3), who argued that this feature is more probably the second harmonic. Although there are slight deviations from the continuum visible in the RXTE-HEXTE and *Suzaku*-GSO data, the signal does not allow us to constrain any parameters. During the giant 2012 November outburst of GRO J1008−57, the signal quality of the *Suzaku*-PIN and -GSO data could be used to additionally investigate this claimed high-energy cyclotron line. These data were not used here since no background data were available at the time of writing. However, Yamamoto et al. (2013) were able to fit the spectra with preliminary background corrections. These authors claimed a cyclotron feature between 74 and 78 keV, close to the feature at 88 keV reported by Shrader et al. (1999).

In conclusion, the fact that the spectrum of several outbursts of GRO J1008−57 can be modeled with the single simple model of Eqs. (4), (6), and (7) shows that the shape and behavior of the spectrum is well understood. Thanks to the flux-independent parameters and the flux correlations found during the analysis (Table 4 and Fig. 10), the spectrum of GRO J1008−57 can be described given only the power-law flux at any time in the subcritial state. This is a remarkable result that has not been seen in any other transient X-ray binary before. GRO J1008−57 therefore shows a well-predictable behavior in outburst dates and spectral shape. Therefore this source is an ideal target on which to clarify more detailed aspects of Be X-ray transients: what drives the peak flux of outbursts? Are there correlations or changes in iron line flux and absorption column density? How can physical models of accretion explain the spectral shape of GRO J1008−57? Are there other sources where similar predictable behavior exists, and are there differences to GRO J1008−57? Does the spectral model of GRO J1008−57 work beyond the flux range covered here?

*Acknowledgements.* We thank the RXTE-, *Swift*- and *Suzaku*-teams for their role in scheduling all observations used within this paper and for accepting our proposals. We especially thank Evan Smith for his help in scheduling the RXTE observations in 2011 April. Many thanks to Hans Krimm for providing the BAT-spectrum during the 2012 giant outburst. We acknowledge funding by the Bundesministerium für Wirtschaft und Technologie under Deutsches Zentrum für Luft- und Raumfahrt grants 50OR0808, 50OR0905, 50OR1113, and the Deutscher Akademischer Austauschdienst. This work has been partially supported by the Spanish Ministerio de Ciencia e Innovación through projects AYA2010-15431 and AIB2010DE-00054. All figures shown in this paper were produced using the `SLXfig` module, developed by John E. Davis. We thank the referee for her/his helpful comments and suggestions.

## References

Becker, P. A., & Wolff, M. T. 2007, ApJ, 654, 435
Becker, P. A., Klochkov, D., Schönherr, G., et al. 2012, A&A, 544, A123
Bildsten, L., Chakrabarty, D., Chiu, J., et al. 1997, ApJS, 113, 367
Boynton, P. E., Deeter, J. E., Lamb, F. K., & Zylstra, G. 1986, ApJ, 307, 545
Caballero, I., & Wilms, J. 2012, Mem. Soc. Astron. It., 83, 230
Caballero, I., Müller, S., Bordas, P., et al. 2012, in SUZAKU 2011: Exploring the X-ray Universe: Suzaku and Beyond, eds. R. Petre, K. Mitsuda, & L. Angelini, AIP Conf. Ser., 1427, 300
Camero-Arranz, A., Finger, M. H., Wilson-Hodge, C. A., et al. 2012, ApJ, 754, 20
Coe, M. J., Roche, P., Everall, C., et al. 1994, MNRAS, 270, L57
Coe, M. J., Bird, A. J., Hill, A. B., et al. 2007, MNRAS, 378, 1427
DeCesar, M. E., Boyd, P. T., Pottschmidt, K., et al. 2013, ApJ, 762, 61
Deeter, J. E., Boynton, P. E., & Pravdo, S. H. 1981, ApJ, 247, 1003
Dickey, J. M., & Lockman, F. J. 1990, ARA&A, 28, 215
Ebisawa, K., Yamauchi, S., Tanaka, Y., Koyama, K., & Suzaku Team 2007, Prog. Theo. Phys. Suppl., 169, 121
Eikmann, W. 2012, Diploma Thesis, Friedrich-Alexander Universität Erlangen-Nürnberg
Ferrigno, C., Becker, P. A., Segreto, A., Mineo, T., & Santangelo, A. 2009, A&A, 498, 825
Finger, M. H., Bildsten, L., Chakrabarty, D., et al. 1999, ApJ, 517, 449
Frank, J., King, A., & Raine, D. 1992, Accretion Power in Astrophysics (Cambridge, UK: Cambridge University Press)
Gehrels, N., Chincarini, G., Giommi, P., et al. 2004, ApJ, 611, 1005
Ghosh, P., & Lamb, F. K. 1979, ApJ, 234, 296
Gnedin, Y. N., & Sunyaev, R. A. 1973, A&A, 25, 233
Godet, O., Beardmore, A. P., Abbey, A. F., et al. 2007, in UV, X-Ray, and Gamma-Ray Space Instrumentation for Astronomy XV, ed. O. H. Siegmund, SPIE Conf. Ser. 6686 (Bellingham: SPIE), 66860
Grove, J. E., Kurfess, J. D., Phlips, B. F., Strickman, M. S., & Ulmer, M. P. 1995, Nuovo Cimento C 19 (Proc. 24th ICRC), 1
Hanke, M. 2011, Ph.D. Thesis, Friedrich-Alexander Universität Erlangen-Nürnberg
Hanke, M., Wilms, J., Nowak, M. A., et al. 2009, ApJ, 690, 330
Hanke, M., Wilms, J., Nowak, M. A., Barragán, L., & Schulz, N. S. 2010, A&A, 509, L8
Horner, W. G. 1819, Phil. Trans. Roy. Soc. London, 109, 308
Houck, J. C., & Denicola, L. A. 2000, in Astronomical Data Analysis Software and Systems IX, eds. N. Manset, C. Veillet, & D. Crabtree, ASP Conf. Ser., 216, 591
Hurkett, C. P., Vaughan, S., Osborne, J. P., et al. 2008, ApJ, 679, 587
Illarionov, A. F., & Sunyaev, R. A. 1975, A&A, 39, 185
Jahoda, K., Markwardt, C. B., Radeva, Y., et al. 2006, ApJS, 163, 401
Kalberla, P. M. W., Burton, W. B., Hartmann, D., et al. 2005, A&A, 440, 775
Kelley, R., Rappaport, S., & Petre, R. 1980, ApJ, 238, 699
Kirsch, M. G., Briel, U. G., Burrows, D., et al. 2005, in UV, X-Ray, and Gamma-Ray Space Instrumentation for Astronomy XIV, ed. O. H. W. Siegmund, SPIE Conf. Ser., 5898, 22
Klochkov, D., Santangelo, A., Staubert, R., & Ferrigno, C. 2008, A&A, 491, 833
Koyama, K., Tsunemi, H., Dotani, T., et al. 2007, PASJ, 59, 23
Krimm, H. A., Barthelmy, S. D., Baumgartner, W., et al. 2012, ATel, 4573
Leahy, D. A., Darbro, W., Elsner, R. F., et al. 1983, ApJ, 266, 160
Levine, A. M., & Corbet, R. 2006, ATel, 940, 1
Levine, A. M., Bradt, H. V., Chakrabarty, D., Corbet, R. H. D., & Harris, R. J. 2011, ApJS, 196, 6
Müller, S., Kühnel, M., Caballero, I., et al. 2012, A&A, 546, A125
Müller, S., Ferrigno, C., Kühnel, M., et al. 2013, A&A, 551, A6
Nagase, F. 1989, PASJ, 41, 1
Naik, S., Paul, B., Kachhara, C., & Vadawale, S. V. 2011, MNRAS, 413, 241
Nakajima, M., Mihara, T., Sugizaki, M., et al. 2012, ATel, 4561
Nowak, M. A., Hanke, M., Trowbridge, S. N., et al. 2011, ApJ, 728, 13

Nowak, M. A., Neilsen, J., Markoff, S. B., et al. 2012, ApJ, 759, 95
Okazaki, A. T., & Negueruela, I. 2001, A&A, 377, 161
Okazaki, A. T., Hayasaki, K., & Moritani, Y. 2013, PASJ, 65, 41
Ostriker, J. P., & Davidson, K. 1973, in X- and Gamma-Ray Astronomy, eds. H. Bradt, & R. Giacconi, IAU Symp., 55, 143
Pottschmidt, K., Suchy, S., Rivers, E., et al. 2012, in SUZAKU 2011: Exploring the X-ray Universe: Suzaku and Beyond, eds. R. Petre, K. Mitsuda, & L. Angelini, AIP Conf. Proc. 1427, 60
Reig, P., & Nespoli, E. 2013, A&A, 551, A1
Revnivtsev, M., Sazonov, S., Churazov, E., et al. 2009, Nature, 458, 1142
Riquelme, M. S., Torrejón, J. M., & Negueruela, I. 2012, A&A, 539, A114
Rothschild, R. E., Blanco, P. R., Gruber, D. E., et al. 1998, ApJ, 496, 538
Schönherr, G., Wilms, J., Kretschmar, P., et al. 2007, A&A, 472, 353
Shrader, C. R., Sutaria, F. K., Singh, K. P., & Macomb, D. J. 1999, ApJ, 512, 920
Stollberg, M. T., Finger, M. H., Wilson, R. B., et al. 1993, IAU Circ., 5836
Takahashi, T., Abe, K., Endo, M., et al. 2007, PASJ, 59, 35
Wilms, J., Allen, A., & McCray, R. 2000, ApJ, 542, 914
Wilms, J., Nowak, M. A., Pottschmidt, K., et al. 2006, A&A, 447, 245
Wilson, R. B., Harmon, B. A., Fishman, G. J., et al. 1994, in The Evolution of X-ray Binaries, eds. S. Holt, & C. S. Day, AIP Conf. Ser., 308, 451
Yamamoto, T., Mihara, T., Sugizaki, M., et al. 2013, ATel, 4759
Yamauchi, S., Ebisawa, K., Tanaka, Y., et al. 2009, PASJ, 61, 225
Yan, J., Li, H., & Liu, Q. 2012, 744, 37

**Table 1.** Log of observations.

| Sat. | Observation | Starttime | Exp. | E |
|---|---|---|---|---|
| Observations in quiescence (1996/1997) | | | | |
| RXTE | 20132-01-01-000 | 50 412.49 | 9439 | I |
| RXTE | 20132-01-01-00 | 50 412.80 | 6623 | I |
| RXTE | 20132-01-01-01 | 50 413.05 | 8719 | I |
| RXTE | 20132-01-01-02 | 50 413.21 | 1136 | I |
| RXTE | 20132-01-01-04 | 50 413.69 | 4319 | I |
| RXTE | 20132-01-01-05 | 50 413.84 | 1472 | I |
| RXTE | 20132-01-02-00 | 50 466.74 | 17 135 | I |
| RXTE | 20132-01-02-01 | 50 467.09 | 4687 | I |
| RXTE | 20132-01-02-02 | 50 467.22 | 5023 | I |
| RXTE | 20132-01-02-03 | 50 467.38 | 3648 | I |
| RXTE | 20132-01-02-04 | 50 467.64 | 7327 | I |
| RXTE | 20132-01-03-000 | 50 514.36 | 13327 | I |
| RXTE | 20132-01-03-00 | 50 514.67 | 9999 | I |
| RXTE | 20132-01-03-01 | 50 514.87 | 10047 | I |
| RXTE | 20132-01-03-02 | 50 515.02 | 11231 | I |
| RXTE | 20123-09-01-00 | 50 519.20 | 4335 | I |
| RXTE | 20123-09-02-00 | 50 537.48 | 4559 | I |
| RXTE | 20123-09-03-00 | 50 565.90 | 5375 | I |
| RXTE | 20132-01-04-00 | 50 567.38 | 15615 | I |
| RXTE | 20132-01-04-03 | 50 568.36 | 9455 | I |
| RXTE | 20132-01-04-01 | 50 569.52 | 7855 | I |
| RXTE | 20132-01-04-02 | 50 569.68 | 9599 | I |
| RXTE | 20132-01-04-04 | 50 569.95 | 1456 | I |
| RXTE | 20123-09-04-00 | 50 602.11 | 4607 | I |
| RXTE | 20123-09-05-00 | 50 619.11 | 4303 | I |
| Outburst in 2005 February | | | | |
| RXTE | 90089-03-01-00 | 53 421.56 | 832 | |
| RXTE | 90089-03-02-01 | 53 426.01 | 2208 | II |
| RXTE | 90089-03-02-08 | 53 426.29 | 863 | II |
| RXTE | 90089-03-02-07 | 53 426.40 | 1232 | II |
| RXTE | 90089-03-02-02 | 53 427.11 | 2912 | III |
| RXTE | 90089-03-02-000 | 53 427.29 | 15536 | III |
| RXTE | 90089-03-02-00 | 53 427.59 | 7792 | III |
| RXTE | 90089-03-02-03 | 53 428.11 | 1808 | IV |
| RXTE | 90089-03-02-04 | 53 428.27 | 5968 | IV |
| RXTE | 90089-03-02-05 | 53 428.84 | 735 | IV |
| RXTE | 90089-03-02-06 | 53 429.28 | 9808 | |
| RXTE | 90089-03-02-09 | 53 430.33 | 7536 | |
| RXTE | 90089-03-02-10 | 53 431.14 | 1376 | V |
| RXTE | 90089-03-02-12 | 53 431.20 | 2896 | V |
| RXTE | 90089-03-02-14 | 53 431.56 | 1248 | V |
| RXTE | 90089-03-02-11 | 53 431.66 | 1360 | V |
| RXTE | 90089-03-02-15 | 53 431.72 | 624 | V |
| RXTE | 90089-03-02-16 | 53 432.12 | 1616 | V |
| RXTE | 90089-03-02-13 | 53 432.18 | 1584 | V |
| Outburst in 2007 December | | | | |
| RXTE | 93032-03-01-00 | 54 426.00 | 560 | |
| *Swift* | 00031030001 | 54 427.69 | 2892 | |
| RXTE | 93032-03-02-00 | 54 427.81 | 2832 | |
| RXTE | 93032-03-02-01 | 54 429.84 | 2016 | |
| RXTE | 93032-03-02-02 | 54 431.61 | 2592 | |
| RXTE | 93032-03-02-03 | 54 433.05 | 1712 | |
| RXTE | 93032-03-03-00 | 54 434.24 | 1520 | |
| Suzaku | 902003010 | 54 434.48 | 34385 | |
| RXTE | 93032-03-03-01 | 54 435.50 | 863 | |
| RXTE | 93032-03-03-02 | 54 437.14 | 560 | |
| RXTE | 93032-03-03-03 | 54 438.17 | 768 | |
| RXTE | 93032-03-03-04 | 54 439.92 | 1760 | |
| RXTE | 93032-03-04-01 | 54 442.12 | 832 | VI |
| RXTE | 93032-03-04-02 | 54 443.10 | 591 | VI |
| RXTE | 93032-03-04-00 | 54 443.79 | 927 | VI |
| RXTE | 93032-03-04-04 | 54 445.23 | 1200 | VII |
| RXTE | 93032-03-04-03 | 54 446.33 | 1184 | VII |
| RXTE | 93032-03-04-06 | 54 447.02 | 1360 | VII |
| RXTE | 93423-02-01-00 | 54 449.18 | 1168 | VIII |
| RXTE | 93423-02-01-01 | 54 451.98 | 1712 | VIII |
| RXTE | 93423-02-01-02 | 54 454.87 | 1616 | VIII |
| RXTE | 93423-02-02-00 | 54 457.16 | 1136 | VIII |
| Outburst in 2011 April | | | | |
| RXTE | 96368-01-03-04 | 55 647.35 | 655 | IX |
| RXTE | 96368-01-03-03 | 55 648.39 | 671 | IX |
| RXTE | 96368-01-03-02 | 55 649.62 | 688 | |
| RXTE | 96368-01-03-01 | 55 650.72 | 944 | |
| RXTE | 96368-01-03-00 | 55 651.97 | 768 | |
| RXTE | 96368-01-02-06 | 55 652.55 | 1104 | |
| RXTE | 96368-01-02-05 | 55 653.66 | 688 | |
| RXTE | 96368-01-02-04 | 55 654.50 | 719 | |
| RXTE | 96368-01-02-03 | 55 655.48 | 671 | |
| RXTE | 96368-01-02-02 | 55 656.59 | 704 | |
| RXTE | 96368-01-02-01 | 55 657.64 | 495 | |
| RXTE | 96368-01-02-07 | 55 658.23 | 1840 | |
| RXTE | 96368-01-02-08 | 55 658.37 | 2352 | |
| RXTE | 96368-01-02-09 | 55 658.43 | 13 024 | |
| RXTE | 96368-01-02-00 | 55 658.72 | 15 744 | |
| RXTE | 96368-01-01-08 | 55 659.15 | 1584 | |
| RXTE | 96368-01-01-05 | 55 659.55 | 6448 | |
| RXTE | 96368-01-01-03 | 55 659.67 | 16 863 | |
| RXTE | 96368-01-01-00 | 55 660.32 | 14 464 | |
| RXTE | 96368-01-01-02 | 55 660.65 | 17 695 | |
| RXTE | 96368-01-01-07 | 55 661.37 | 2432 | |
| RXTE | 96368-01-01-01 | 55 661.43 | 14 224 | |
| RXTE | 96368-01-01-06 | 55 661.96 | 655 | |
| Outburst in 2011 December | | | | |
| *Swift* | 00031030002 | 55 915.83 | 1994 | |
| *Swift* | 00031030003 | 55 917.05 | 1801 | |
| *Swift* | 00031030004 | 55 918.78 | 1344 | |
| *Swift* | 00031030005 | 55 919.91 | 2032 | |
| After outburst in 2011 December | | | | |
| *Swift* | 00031030006 | 55 932.08 | 1044 | |
| *Swift* | 00031030007 | 55 934.49 | 1196 | |
| *Swift* | 00031030009 | 55 938.77 | 969 | |
| *Swift* | 00031030010 | 55 940.42 | 986 | |
| *Swift* | 00031030011 | 55 955.80 | 1081 | |
| *Swift* | 00031030012 | 55 958.14 | 1039 | |
| "Giant" outburst in November 2012 | | | | |
| *Swift* | 00031030013 | 56 196.99 | 4533 | |
| *Swift* | 00538290000 | 56 244.91 | 3017 | |
| *Swift* | 00031030014 | 56 246.18 | 1982 | |
| *Swift* | 00031030015 | 56 248.25 | 1308 | |
| *Swift* | 00031030016 | 56 250.18 | 2021 | |
| Suzaku | 907006010 | 56 251.63 | 6521 | |
| *Swift* | 00031030017 | 56 252.59 | 2007 | |

**Notes.** The table includes the satellite used (Sat.), the observation ID, the modified Julian date of the start of observation, and the exposure (Exp.) in seconds. The last column (E) marks data epochs for which spectra were combined for spectral analysis. Horizontal lines separate different outbursts or campaigns.